JANUARY 13 2026

Homogenization of resonant bubble screens: Influence of bubble shape and lattice arrangement

Kim Pham ; Agnès Maurel

J. Acoust. Soc. Am. 159, 357–372 (2026)
https://doi.org/10.1121/10.0041877

JASA ARTICLE

Homogenization of resonant bubble screens: Influence of bubble shape and lattice arrangement

Kim Pham[1,2,a] and Agnès Maurel[2,b]

[1]*Laboratoire de Mécanique et d'Ingénierie (LMI), ENSTA Paris (École Nationale Supérieure de Techniques Avancées Paris), Institut Polytechnique de Paris, 91120 Palaiseau, France*

[2]*Institut Langevin, CNRS (Centre National de la Recherche Scientifique), ESPCI ParisTech (École Supérieure de Physique et de Chimie Industrielles de la Ville de Paris), Université PSL (Paris Sciences & Letters), 75005 Paris, France*

ABSTRACT:

A time-domain effective model for acoustic wave propagation through a two-dimensional periodic array of gas bubbles embedded in a liquid is presented. The model is expressed as transmission conditions: pressure remains continuous, whereas the normal velocity exhibits a jump induced by the internal pressure of the bubbles. This internal pressure follows a damped mass–spring equation, with damping arising solely from radiative coupling to the surrounding liquid, which makes the resonance frequency and quality factor of the array emerge unambiguously. Aside from the bubble density in the lattice, these quantities are fully governed by two independent geometric parameters: a dimensionless capacitance, depending solely on bubble shape, and a lattice coefficient, depending solely on lattice geometry. For plane wave scattering, comparisons with direct numerical simulations demonstrate that the model accurately reproduces the resonant behavior of bubble screens across a range of configurations, including spherical, spheroidal, and cylindrical bubbles, as well as square and rectangular lattices. This generalizes the classical model of Leroy *et al.* [Eur. Phys. J. E **29**(1), 123–130 (2009)] for spherical bubbles in square lattices. Notably, the model reveals—and simulations confirm—that the resonance frequency shift relative to an isolated bubble, usually positive (blue shift), can become negative (red shift) in rectangular lattices with aspect ratios exceeding seven.

 https://doi.org/10.1121/10.0041877

(Received 4 September 2025; revised 24 November 2025; accepted 1 December 2025; published online 13 January 2026)

[Editor: Charles C. Church]]

Pages: 357–372

I. INTRODUCTION

Gas bubbles embedded in a liquid exhibit remarkable acoustic properties, especially near their Minnaert resonance, attributable to the large contrast in compressibility between gas and liquid (Minnaert, 1933). An original and insightful historical review of studies on scattering by single bubbles, including foundational works and those conducted during World War II, is provided by Martin (2019). Building on this property, bubble-based acoustic metasurfaces, which are also referred to as bubble metascreens, have attracted increasing attention because of their ability to manipulate sound at deeply subwavelength scales (Hladky-Hennion and Decarpigny, 1991; Leroy *et al.*, 2009; Bretagne *et al.*, 2011). Such systems, consisting of two-dimensional, periodic or quasiperiodic arrays of air bubbles in water, form ultrathin interfaces capable of achieving functionalities such as superabsorption (Leroy *et al.*, 2015; Ammari *et al.*, 2017a), coherent perfect absorption (CPA; Lanoy *et al.*, 2018), and subwavelength focusing (Lanoy *et al.*, 2015; Ammari *et al.*, 2017b). These effects arise from the collective dynamics of the bubbles, which are governed by various mechanisms related to array density, bubble shape, and lattice geometry.

Although most studies have focused on spherical bubbles, it is now well established that bubble shape plays a critical role in modulating the resonance. For a single bubble, deviations from sphericity alter the pressure and velocity distribution at the interface, leading to measurable shifts in resonance frequency—theoretically and experimentally—for shapes such as spheroidal (Strasberg, 1953; Ye, 1997; Spratt *et al.*, 2017) or toroidal/polyhedral bubbles (Boughzala *et al.*, 2021; Alloul *et al.*, 2022; Bouchet *et al.*, 2024). These geometric effects can be described quantitatively through the concept of capacitance, borrowed from electrostatics (Smythe, 1950), which characterizes how bubble shape influences the pressure–volume response and, thus, shifts its Minnaert resonance frequency. A rigorous connection between the scattering properties of a bubbly metascreen and the capacitance of its resonators was established in Ammari *et al.* (2017a), employing layer potential techniques and asymptotic expansions to analyze bubbles mounted on a Dirichlet surface; see also Martin and Skvortsov (2020) for sound-hard and sound-soft scatterers. Another factor affecting the array's response, in terms of resonance frequency and quality factor, is the geometric effect of the lattice arrangement, independent of

[a]Email: kim.pham@ensta.fr
[b]Email: agnes.maurel@espci.fr

bubble shape. To our knowledge, this influence has not been investigated in the literature, where the square arrangement is always assumed by default.

In this work, we develop a model that faithfully describes the response of a bubble array for arbitrary bubble shapes and lattice arrangements. In particular, we show that the array's resonance frequency can be expressed as

$$\omega_r = \frac{\omega_r^\infty}{\sqrt{1-\Gamma_\circ \Gamma_{\mathrm{L}}(d/h)}} \quad \text{for a screen,} \tag{1}$$

where

$$\omega_r^\infty = \frac{c_g}{d}\sqrt{\Gamma_\circ \frac{\rho_g}{\rho_\ell}} \quad \text{for a single bubble.} \tag{2}$$

Here, (ρ_g, ρ_ℓ) denote the gas and liquid densities, respectively, c_g is the sound speed in the gas, $d^3 = V$ is the bubble volume, and $h^2 = S$ is the lattice surface of the array. Next, $\Gamma_\circ > 0$ is the dimensionless *bubble capacitance*, influencing ω_r^∞, the Minnaert resonance frequency of a single bubble in free space, and Γ_{L} is the *lattice parameter*, which depends only on the lattice geometry and produces an additional frequency shift. Importantly, we will show that Γ_{L} can be either positive or negative. As a result—challenging the common perception in the literature that lattice effects invariably cause a blue shift (upshift) of the array resonance compared to an isolated bubble—we show that the bubble array can also exhibit a red shift (downshift).

Our model is derived using homogenization combined with matched asymptotic expansions, a powerful framework for obtaining effective descriptions of wave scattering by thin, structured arrays in the low-frequency regime. This combined homogenization–asymptotic framework was initially developed in the quasi-static context and later extended to dynamic problems in acoustics and elasticity (Delourme *et al.*, 2012; Marigo and Maurel, 2016; Pham *et al.*, 2021a). It has since been applied to ultrathin resonant metasurfaces operating in the deep-subwavelength regime, including acoustic, optical, elastic, and water-wave configurations (Tachet *et al.*, 2025; Lebbe *et al.*, 2023; Marigo *et al.*, 2021; Euvé *et al.*, 2021; Schnitzer and Brandão, 2022). Earlier homogenization-based approaches were developed for three-dimensional bubbly media, most notably the effective propagation models of Caflisch *et al.* (1985) and their extension by Miksis and Ting (1989) to thin bubbly layers. These treatments rely on volume homogenization and do not resolve the microscopic structure of a two-dimensional bubble screen. In the context of bubbly screens, a fully matched asymptotic treatment was introduced in Pham *et al.* (2021b) to derive nonlinear jump conditions and a nonlinear resonator equation for a square array of spherical bubbles. The present work revisits the problem in the linear regime and significantly extends its scope by capturing bubble shape and lattice-arrangement effects. A key strength of the approach lies in its generality: the array density is an explicit parameter, the bubble shape enters exclusively through its capacitance, and the lattice arrangement is encoded in the lattice parameter—determined from auxiliary static problems.

The paper is organized as follows. Section II introduces the physical configuration and summarizes the main asymptotic results, including the damped-oscillator equation governing the bubble pressure, where the damping originates from the array's radiative losses (thus, defining, unambiguously, the resonance frequency and quality factor). Section III details the derivation of the effective model via matched asymptotic expansions and homogenization, leading to the results stated in Sec. II. Section IV examines the bubble screen's scattering behavior and validates the model against direct numerical simulations for a variety of array densities, bubble shapes, and lattice arrangements. Conclusions and perspectives are given in Sec. V. In two appendixes, we collect (i) technical results and remarks on the parameters $(\Gamma_\circ, \Gamma_{\mathrm{L}})$, in particular, how they are computed numerically; and (ii) a comparison with the well-established model of Leroy *et al.* (2009) for spherical bubbles in a square lattice.

II. SETTING OF THE PROBLEM AND SUMMARY OF THE MAIN RESULTS

We consider a two-dimensional array of gas bubbles embedded in a liquid, periodically distributed on the plane $x = 0$; see Fig. 1. The cross-sectional area of the unit cell is S and the volume of each bubble is V. In the actual configuration, the velocity $\boldsymbol{u}$ and pressure p satisfy the linearized Euler equations

$$\rho \frac{\partial \boldsymbol{u}}{\partial t} = -\nabla p, \qquad \mathrm{div}\boldsymbol{u} + \frac{1}{\rho c^2}\frac{\partial p}{\partial t} = 0, \tag{3}$$

where $(\rho, c) = (\rho_\ell, c_\ell)$ in the liquid and $(\rho, c) = (\rho_g, c_g)$ inside the gas. At the bubble–liquid interfaces, the pressure and normal velocity are continuous.

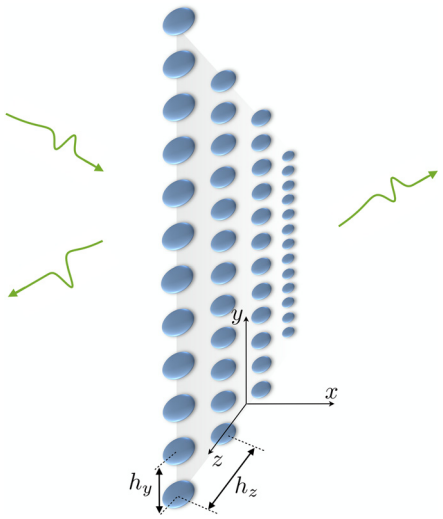

FIG. 1. Wave scattering by an acoustic bubble screen, consisting of a periodic array of gas bubbles in a liquid governed by Eq. (3). We denote $V = d^3$ for the volume of each bubble and $S = h_y h_z = h^2$ for the lattice surface of the array.

https://doi.org/10.1121/10.0041877

A. Effective behavior of the pressure field in the liquid and gas

The homogenization of the above system in the subwavelength regime yields an effective problem posed solely in the liquid, where the bubble screen is replaced by homogenized jump conditions across the interface $x = 0$. Let $(\overline{\boldsymbol{u}}, \overline{p})$ denote the homogenized velocity and pressure fields in the liquid. These satisfy

$$\rho_\ell \frac{\partial \overline{\boldsymbol{u}}}{\partial t} = -\nabla \overline{p}, \qquad \operatorname{div} \overline{\boldsymbol{u}} + \frac{1}{\rho_\ell c_\ell^2} \frac{\partial \overline{p}}{\partial t} = 0 \ \text{ for } x \neq 0, \tag{4}$$

together with the continuity of pressure across $x = 0$ and a jump in the normal velocity coupled to a mass-spring resonator equation

$$\begin{cases} [\![\, \overline{p} \,]\!] = 0, \quad [\![\overline{u}_x]\!] = -\dfrac{d^3}{\rho_g c_g^2 h^2} \dfrac{\partial p_r}{\partial t}, \\ \dfrac{\partial^2 p_r}{\partial t^2} + \omega_r^2 p_r = \omega_r^2 \ \overline{p}_{|x=0}, \end{cases} \tag{5}$$

where $[\![v]\!] = v_{|x=0^+} - v_{|x=0^-}$ and

$$\omega_r = \frac{c_g}{d} \sqrt{\frac{\Gamma_\circ}{1 - \Gamma_\circ \Gamma_{\mathrm{L}} (d/h)} \frac{\rho_g}{\rho_\ell}} \tag{6}$$

is the resonance frequency of the bubble screen, as introduced in Eqs. (1) and (2). Here, $h = S^{1/2}$ and $d = V^{1/3}$ are the characteristic length scales associated with the array periodicity and bubble size, respectively. The auxiliary field $p_r(y, z, t)$ in Eq. (5), defined along the screen, represents the homogenized gas pressure inside the bubbles under the action of the pressure $\overline{p}$ in the liquid (where $\overline{p}_{|x=0}$ is its restriction to the plane $x = 0$).

In Eq. (5), the effective jump conditions are precisely the linearized counterparts of those derived in our previous homogenization study (Pham *et al.*, 2021b), and the resonator equation governing p_r is the linearized form of the nonlinear Rayleigh–Plesset equation obtained in that same work. In that earlier work, these relations were established for spherical bubbles arranged in a square lattice; the present study generalizes them to bubbles of arbitrary shape and arbitrary lattice geometries. Equations (4) and (5) apply in the subwavelength regime, meaning that the lattice spacing h is small compared with the characteristic acoustic wavelength. They also assume a sparse array, i.e., a bubble size d that is much smaller than h. This is not a restriction of the homogenized model itself but rather a physical requirement for the Minnaert-type resonance to be observable: dense (non-sparse) arrays suppress the resonance and behave, instead, as nearly perfectly reflecting surfaces because of the strong density contrast of the bubbles.

B. Definitions of $\Gamma_\circ$ and Γ_{L}

The parameters $\Gamma_\circ$ and Γ_{L} are dimensionless geometric quantities obtained from the asymptotic analysis presented in Sec. III. The capacitance $\Gamma_\circ > 0$ depends solely on the shape of the bubbles, whereas the lattice parameter Γ_{L} depends only on the lattice arrangement (e.g., square, rectangular, or hexagonal). Their computation relies on the resolution of two independent elementary problems:

- Lattice parameter Γ_{L}:
  Let Ω_{m} be a guide of *unitary cross-sectional area* Σ_{m}, matching the cross section of the considered lattice, and let $\boldsymbol{r}_{\mathrm{m}} = \boldsymbol{r}/h$ denote the associated rescaled coordinate [Fig. 2(a)]. We define the Green's function $G_{\mathrm{L}} : \Omega_{\mathrm{m}} \to \mathbb{R}$ for the guide Ω_{m} with a singularity at the origin as the unique solution of the Laplace boundary-value problem such that

$$\begin{cases} \Delta G_{\mathrm{L}} = 0 \ \text{ in } \Omega_{\mathrm{m}}, \\ G_{\mathrm{L}} \text{ periodic}, \quad \nabla G_{\mathrm{L}} \cdot \boldsymbol{n} \text{ anti} - \text{periodic on } \partial\Omega_{\mathrm{m}}, \\ \lim\limits_{x_{\mathrm{m}} \to \pm\infty} \left(G_{\mathrm{L}} - \dfrac{|x_{\mathrm{m}}|}{2} \right) = 0, \quad \nabla G_{\mathrm{L}} \underset{r_{\mathrm{m}} \to 0}{\sim} \dfrac{\boldsymbol{e}_r}{4\pi r_{\mathrm{m}}^2}, \end{cases} \tag{7}$$

  where $\boldsymbol{n}$ is the outward unit normal to the lateral boundary $\partial\Omega_{\mathrm{m}}$, $x_{\mathrm{m}} = \boldsymbol{r}_{\mathrm{m}} \cdot \boldsymbol{e}_x$ and $r_{\mathrm{m}} = |\boldsymbol{r}_{\mathrm{m}}|$. Then, the constant Γ_{L} is defined as

$$\Gamma_{\mathrm{L}} = \lim_{r_{\mathrm{m}} \to 0} \left(G_{\mathrm{L}} + \frac{1}{4\pi r_{\mathrm{m}}} \right). \tag{8}$$

  Note. Because the singularity is located at the origin, G_{L} is, by construction, an even function of y_m and z_m. This symmetry simplifies the computation of G_{L} as the periodic boundary conditions on $\partial\Omega_{\mathrm{m}}$ in Eq. (7) may be replaced with homogeneous Neumann conditions, $\nabla G_{\mathrm{L}} \cdot \boldsymbol{n} = 0$ on $\partial\Omega_{\mathrm{m}}$.
- Bubble parameter (capacitance) $\Gamma_\circ$:
  Let $\Omega_\mu^{\mathrm{gas}}$ be a bubble of *unit volume* embedded in $\Omega_\mu = \mathbb{R}^3$, and $\boldsymbol{r}_\mu = \boldsymbol{r}/d$ are the associated rescaled coordinates [Fig. 2(b)]. We define the field $G_\circ : \Omega_\mu^{\mathrm{liq}} \to \mathbb{R}$, where $\Omega_\mu^{\mathrm{liq}} = \Omega_\mu \backslash \Omega_\mu^{\mathrm{gas}}$ is the surrounding liquid region, as the unique solution of the Laplace boundary-value problem

$$\begin{cases} \Delta G_\circ = 0 \text{ in } \Omega_\mu^{\mathrm{liq}}, \ G_\circ = 0 \text{ on } \partial\Omega_\mu^{\mathrm{gas}}, \\ \lim\limits_{r_\mu \to +\infty} \nabla G_\circ = \dfrac{\boldsymbol{e}_r}{4\pi r_\mu^2}, \end{cases} \tag{9}$$

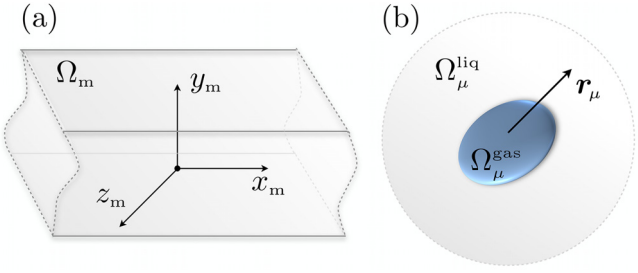

FIG. 2. (a) Mesoscopic domain Ω_{m} is a guide of unitary cross section, infinite along $\boldsymbol{e}_x$ with periodic boundary conditions on its lateral boundaries; $\boldsymbol{r}_{\mathrm{m}} = (x_{\mathrm{m}}, y_{\mathrm{m}}, z_{\mathrm{m}})$ where $\boldsymbol{r}_{\mathrm{m}} = \boldsymbol{r}/h$. (b) Microscopic domain is a gas bubble $\Omega_\mu^{\mathrm{gas}}$ of unitary volume surrounded by an infinite liquid region $\Omega_\mu^{\mathrm{liq}}$; $\boldsymbol{r}_\mu = \boldsymbol{r}/d$.

with $r_\mu = |r_\mu|$. The constant $\Gamma_\circ$ is then given by

$$\frac{1}{\Gamma_\circ} = \lim_{r_\mu \to +\infty} \left(G_\circ + \frac{1}{4\pi r_\mu} \right) \geq 0 \tag{10}$$

(see Appendix A 1 for its correspondence with the electrostatic capacitance of a conductor and for the proof of its positivity).

Appendix A 2 details how $\Gamma_\circ$ and Γ_L are computed numerically using standard finite element method.

C. Resonance quality factor

In Eq. (5), p_r represents the homogenized version of the pressure inside the bubbles. Because these bubbles are coupled to the surrounding liquid, a radiative damping term is expected to appear. This term is actually "hidden" in $\overline{p}_{|x=0}$ (which depends on p_r), but it can be made explicit by considering a wave propagating in the direction $(\cos\theta, \sin\theta\cos\varphi, \sin\theta\sin\varphi)$ of the form $p^{\text{inc}}(t - \mathrm{x}^+/c_\ell)$, where $\mathrm{x}^+ = x\cos\theta + \sin\theta(y\cos\varphi + z\sin\varphi)$. Then, the solution can be written as

$$\overline{p}(x,y,z,t) = p^{\text{inc}}\left(t - \mathrm{x}^+/c_\ell\right) + \begin{cases} f(t + \mathrm{x}^-/c_\ell), & x \leq 0, \\ f\left(t - \mathrm{x}^+/c_\ell\right), & x > 0, \end{cases} \tag{11}$$

where $\mathrm{x}^- = x\cos\theta - \sin\theta(y\cos\varphi + z\sin\varphi)$. By using the same function f for $x > 0$ and $x < 0$, the pressure $\overline{p}$ is continuous at $x = 0$ as required by Eq. (5). Applying the jump condition on the normal velocity component u_x given in Eq. (5) then leads to

$$f' = -\frac{1}{2\cos\theta} \frac{\rho_\ell c_\ell}{\rho_g c_g^2} \frac{d^3}{h^2}\ p_r, \tag{12}$$

where f' denotes the derivative of f. Substituting this expression of $\overline{p}$ into the resonator equation in Eq. (5) then yields the equivalent form

$$\frac{\partial^2 p_r}{\partial t^2} + \frac{2\omega_r}{Q}\ \frac{\partial p_r}{\partial t} + \omega_r^2 p_r = \omega_r^2\ p^{\text{inc}}_{|x=0}, \tag{13}$$

with, now, a source term independent of p_r. The quality factor Q appears explicitly, measuring the radiative damping caused by the coupling between the resonator and surrounding liquid,

$$Q = 4\cos\theta \sqrt{\frac{\rho_g c_g^2}{\rho_\ell c_\ell^2}} \sqrt{\frac{1 - \Gamma_\circ \Gamma_L (d/h)}{\Gamma_\circ}} \left(\frac{h}{d}\right)^2. \tag{14}$$

The quality factor increases when moving from a compact array to a sparse arrat, whereas the resonance frequency of the bubble screen approaches that of a single, isolated bubble—an expected and general result (see, for example, Maurel *et al.*, 2019, and Tachet *et al.*, 2025). This behavior has been associated with super-radiation (Leroy *et al.*, 2009; Leroy *et al.*, 2015) as the quality factor is larger by a factor of $(h/d)^2 \gg 1$ compared to the quality factor $q \simeq \sqrt{\rho_g c_g^2/\rho_\ell c_\ell^2}$ of an isolated bubble (Devin, 1959; Prosperetti, 1977).

III. ASYMPTOTIC DERIVATION OF THE EFFECTIVE PROBLEM

We begin by introducing the nondimensional form of the governing equations through the change of variables

$$\begin{aligned} &t \to \omega t, \quad \boldsymbol{r} \to k\boldsymbol{r}, \quad \rho \to \rho/\rho_\ell, \quad c \to c/c_\ell, \\ &\boldsymbol{u} \to \boldsymbol{u}/c_\ell, \quad p \to p/(\rho_\ell c_\ell^2), \end{aligned} \tag{15}$$

where ω denotes the typical excitation frequency and $k = \omega/c_\ell$ is the corresponding wavenumber. Defining the dimensionless parameters $A = \rho_\ell/\rho$ and $B = \rho_\ell c_\ell^2/\rho c^2$, the linearized Euler equations take the form

$$\frac{\partial \boldsymbol{u}}{\partial t} = -A\nabla p, \qquad \operatorname{div}\boldsymbol{u} + B\frac{\partial p}{\partial t} = 0, \tag{16}$$

where $(A,B) = (1,1)$ in the liquid and $(A,B) = (\rho_\ell/\rho_g, \rho_\ell c_\ell^2/\rho_g c_g^2)$ in the gas. Because our objective is to derive the homogenized description in the low-frequency regime—relevant here because the Minnaert resonance occurs in the subwavelength domain—we introduce the small parameter

$$\eta = kh \ll 1.$$

Following the scaling assumptions of Pham *et al.* (2021b), we adopt

$$\frac{\rho_g}{\rho_\ell} \sim \eta^4, \qquad \frac{d}{h} \sim \eta,$$

and $c_g/c_\ell = O(1)$. These scalings, corresponding to a dilute array of bubbles with a strong density contrast, ensure that the analysis remains in the resonant regime as $\eta \to 0$, where $\omega_r h/c_\ell = O(kh) = O(\eta)$. In this regime, the bubble array operates near its Minnaert resonance, as $\omega_r h/c_\ell \sim (h/d)(c_g/c_\ell)\sqrt{\rho_g/\rho_\ell}$ from Eqs. (1) and (2). Accordingly, we write the nondimensional constitutive parameters as

$$(A,B) = \begin{cases} (1,1) & \text{in the liquid,} \\ \left(\dfrac{\alpha}{\eta^4}, \dfrac{\beta}{\eta^4}\right), \quad (\alpha,\beta) = O(1) & \text{in the gas.} \end{cases}$$

A. Multiscale setting

We distinguish three spatial scales: macroscopic, mesoscopic, and microscopic. The corresponding coordinates are defined as

$$\text{macro}: \boldsymbol{r}, \quad \text{meso}: \boldsymbol{r}_{\text{m}} = \frac{\boldsymbol{r}}{\eta}, \quad \text{micro}: \boldsymbol{r}_\mu = \frac{\boldsymbol{r}}{\ell\eta^2},$$

where $\ell = d/(\eta h) = O(1)$ is chosen such that the bubble has unit volume at the microscopic scale. In other words, $\boldsymbol{r}$ is

https://doi.org/10.1121/10.0041877

scaled with the typical wavelength $1/k$, $\boldsymbol{r}_{\mathrm{m}}$ is scaled with the periodicity h, and $\boldsymbol{r}_\mu$ is scaled with the bubble size d.

The macroscopic domain – At the macroscopic scale, the fields are expanded as follows:

$$\boldsymbol{u} = \sum_{n\geq 0} \eta^n \boldsymbol{u}^{(n)}(\boldsymbol{r},t), \quad p = \sum_{n\geq 0} \eta^n p^{(n)}(\boldsymbol{r},t), \tag{17}$$

where $(\boldsymbol{u}^{(n)}, p^{(n)})$ is defined for $x \neq 0$. Substituting these expansions into Eq. (16) yields, at each order, the macroscopic equations

$$\frac{\partial \boldsymbol{u}^{(n)}}{\partial t} = -\boldsymbol{\nabla} p^{(n)}, \quad \operatorname{div} \boldsymbol{u}^{(n)} + \frac{\partial p^{(n)}}{\partial t} = 0, \tag{18}$$

supplemented by transmission conditions for $(u_x^{(n)}, p^{(n)})$ across the interface $x = 0$, which remain to be determined. The truncation of the series [Eq. (17)] at order one yields the macroscopic (homogenized) fields $(\overline{u}, \overline{p})$ introduced in Eq. (5).

The mesoscopic domain – The mesoscopic domain Ω_{m}, illustrated in Fig. 2(a), is obtained by zooming in by a factor of $1/\eta$ around a point of the interface located at $\boldsymbol{r} = (0, \boldsymbol{r}_\parallel)$, where $\boldsymbol{r}_\parallel = (y,z)$ denotes the coordinates tangential to the screen. Using the rescaled coordinates $\boldsymbol{r}_{\mathrm{m}} = (x_{\mathrm{m}}, y_{\mathrm{m}}, z_{\mathrm{m}})$, the domain is defined as

$$\Omega_{\mathrm{m}} = \left\{ \boldsymbol{r}_{\mathrm{m}} \in \mathbb{R}^3 \,|\, x_{\mathrm{m}} \in (-\infty, +\infty), (y_{\mathrm{m}}, z_{\mathrm{m}}) \in \Sigma_{\mathrm{m}} \right\},$$

where Σ_{m} is the periodic cross section of unitary area. At this scale, the pressure and velocity fields are expanded as

$$\boldsymbol{u} = \sum_{n\geq 0} \eta^n \boldsymbol{u}_{\mathrm{m}}^{(n)}(\boldsymbol{r}_{\mathrm{m}}, \cdot), \quad p = \sum_{n\geq 0} \eta^n p_{\mathrm{m}}^{(n)}(\boldsymbol{r}_{\mathrm{m}}, \cdot), \tag{19}$$

where all fields are taken to be periodic on $\partial\Omega_{\mathrm{m}}$. To simplify the notation, we have defined

$$f(\boldsymbol{r}_{\mathrm{m}}, \cdot) = f(\boldsymbol{r}_{\mathrm{m}}, \boldsymbol{r}_\parallel, t).$$

Following the chain rules, the differential operator is expressed as

$$\boldsymbol{\nabla} \to \boldsymbol{\nabla}_\parallel + \frac{1}{\eta} \boldsymbol{\nabla}_{\mathrm{m}},$$

where $\boldsymbol{\nabla}_\parallel = (\partial/\partial \boldsymbol{r}_\parallel)$ and $\boldsymbol{\nabla}_{\mathrm{m}} = (\partial/\partial \boldsymbol{r}_{\mathrm{m}})$.

Substituting Eq. (19) into Eq. (16) yields, on collecting terms of equal order in η, a hierarchy of equations. At leading orders, these equations read

$$\boldsymbol{0} = -\boldsymbol{\nabla}_{\mathrm{m}} p_{\mathrm{m}}^{(0)}, \quad \frac{\partial \boldsymbol{u}_{\mathrm{m}}^{(0)}}{\partial t} = -\boldsymbol{\nabla}_\parallel p_{\mathrm{m}}^{(0)} - \boldsymbol{\nabla}_{\mathrm{m}} p_{\mathrm{m}}^{(1)}, \tag{20a}$$

$$\operatorname{div}_{\mathrm{m}} \boldsymbol{u}_{\mathrm{m}}^{(0)} = 0, \quad \operatorname{div}_\parallel \boldsymbol{u}_{\mathrm{m}}^{(0)} + \operatorname{div}_{\mathrm{m}} \boldsymbol{u}_{\mathrm{m}}^{(1)} + \frac{\partial p_{\mathrm{m}}^{(0)}}{\partial t} = 0. \tag{20b}$$

At the mesoscopic scale, the bubble reduces to a point at the origin $\boldsymbol{r}_{\mathrm{m}} = \boldsymbol{0}$, such that the behavior of the fields in its vicinity is governed by singular spherical harmonics. In particular, at the dominant orders, the velocity field near the origin is expected to have the form

$$\boldsymbol{u}_{\mathrm{m}}^{(0)}(\boldsymbol{r}_{\mathrm{m}}, \cdot) \underset{r_{\mathrm{m}}\to 0}{\sim} \Phi^{(0)}(\cdot) \frac{\boldsymbol{e}_r}{4\pi r_{\mathrm{m}}^2},$$

$$\boldsymbol{u}_{\mathrm{m}}^{(1)}(\boldsymbol{r}_{\mathrm{m}}, \cdot) \underset{r_{\mathrm{m}}\to 0}{\sim} \Phi^{(1)}(\cdot) \frac{\boldsymbol{e}_r}{4\pi r_{\mathrm{m}}^2} + \frac{\boldsymbol{\psi}^{(1)}(\theta_{\mathrm{m}}, \varphi_{\mathrm{m}}, \cdot)}{r_{\mathrm{m}}^3}, \tag{21}$$

where $\boldsymbol{e}_r$ is the radial unit vector in the spherical coordinate system $(r_{\mathrm{m}}, \theta_{\mathrm{m}}, \varphi_{\mathrm{m}})$ centered at the bubble. The scalars $\Phi^{(n)}(\boldsymbol{r}_\parallel, t)$, $n = 0, 1$, depend only on the macroscopic tangential position $\boldsymbol{r}_\parallel$ and time t, whereas the vector $\boldsymbol{\psi}^{(1)}(\theta_{\mathrm{m}}, \varphi_{\mathrm{m}}, \boldsymbol{r}_\parallel, t)$ also depends on the angular variables. The latter satisfies the zero-mean condition

$$\int_{\theta_{\mathrm{m}}=0}^{\pi} \int_{\varphi_{\mathrm{m}}=0}^{2\pi} \boldsymbol{\psi}^{(1)}(\theta_{\mathrm{m}}, \varphi_{\mathrm{m}}, \boldsymbol{r}_\parallel, t) \cdot \boldsymbol{e}_r \sin\theta_{\mathrm{m}} \, \mathrm{d}\theta_{\mathrm{m}} \mathrm{d}\varphi_{\mathrm{m}} = 0.$$

The microscopic domain – The microscopic domain is obtained by zooming in on the origin $\boldsymbol{r}_{\mathrm{m}} = \boldsymbol{0}$ of the mesoscopic scale, with a magnification factor of $1/(\ell\eta)$. At this scale, the bubble region $\Omega_\mu^{\mathrm{gas}}$ has unit volume and is surrounded by an unbounded liquid region $\Omega_\mu^{\mathrm{liq}}$, which extends infinitely in all three spatial directions. We denote by $\Omega_\mu = \Omega_\mu^{\mathrm{gas}} \cup \Omega_\mu^{\mathrm{liq}} = \mathbb{R}^3$ the union of these two regions, which together constitute the microscopic domain, and $\boldsymbol{r}_\mu$ is the spatial coordinate associated with this scale. In this region, the fields are expanded as

$$\text{in } \Omega_\mu^{\mathrm{liq}}:$$

$$\boldsymbol{u} = \frac{1}{\eta^2} \sum_{n\geq 0} \eta^n \boldsymbol{u}_\mu^{(n)}(\boldsymbol{r}_\mu, \cdot), \quad p = \sum_{n\geq 0} \eta^n p_\mu^{(n)}(\boldsymbol{r}_\mu, \cdot),$$

$$\text{in } \Omega_\mu^{\mathrm{gas}}:$$

$$\boldsymbol{u} = \frac{1}{\eta^2} \sum_{n\geq 0} \eta^n \widetilde{\boldsymbol{u}}_\mu^{(n)}(\boldsymbol{r}_\mu, \cdot), \quad p = \sum_{n\geq 0} \eta^n \widetilde{p}_\mu^{(n)}(\boldsymbol{r}_\mu, \cdot). \tag{22}$$

As previously, we have defined

$$f(\boldsymbol{r}_\mu, \cdot) = f(\boldsymbol{r}_\mu, \boldsymbol{r}_\parallel, t).$$

To simplify the presentation, we have anticipated in Eq. (22) that the velocities in $\Omega_\mu^{\mathrm{gas}}$ and $\Omega_\mu^{\mathrm{liq}}$ begin at order η^{-2}. Applying the chain rule, the differential operator becomes

$$\boldsymbol{\nabla} \to \boldsymbol{\nabla}_\parallel + \frac{1}{\ell\eta^2} \boldsymbol{\nabla}_\mu,$$

where $\boldsymbol{\nabla}_\mu = \partial/\partial \boldsymbol{r}_\mu$.

Substituting the expansions [Eq. (22)] into Eq. (16) and collecting terms of equal powers in η yields the leading-order systems

$$\text{in } \Omega_\mu^{\mathrm{gas}}:$$

$$\boldsymbol{\nabla}_\mu \widetilde{p}_\mu^{(n)} = \boldsymbol{0}, \quad \operatorname{div}_\mu \widetilde{\boldsymbol{u}}_\mu^{(n)} + \ell\beta \frac{\partial \widetilde{p}_\mu^{(n)}}{\partial t} = 0, \quad n = 0, 1; \tag{23}$$

in $\Omega_\mu^{\rm liq}$:

$$\ell \frac{\partial \boldsymbol{u}_\mu^{(n)}}{\partial t} = -\boldsymbol{\nabla}_\mu p_\mu^{(n)}, \quad \mathrm{div}_\mu \boldsymbol{u}_\mu^{(n)} = 0, \quad n = 0, 1, \tag{24}$$

together with continuity conditions at the interface between the liquid and gas such that

$$p_\mu^{(n)} = \widetilde{p}_\mu^{(n)}, \quad \boldsymbol{u}_\mu \cdot \boldsymbol{n} = \widetilde{\boldsymbol{u}}_\mu \cdot \boldsymbol{n} \quad \text{on } \partial\Omega_\mu^{\rm gas}, \tag{25}$$

where $\boldsymbol{n}$ is the outward normal to $\partial\Omega_\mu^{\rm gas}$.

B. The connection between the macro- and meso-scales: Jump conditions

To derive the transmission conditions at $x = 0$ on the macroscopic scale, we connect the macroscopic and mesoscopic regions by matching their respective expansions [Eqs. (22) and (19)] in an intermediate region where $x \to 0^\pm$ and $x_{\rm m} \to \pm\infty$ such that

$$p^{(0)}(\boldsymbol{r}, t) + \eta p^{(1)}(\boldsymbol{r}, t) + \cdots \underset{\substack{x \to 0^\pm \\ x_{\rm m} \to \pm\infty}}{\sim} p_{\rm m}^{(0)}(\boldsymbol{r}_{\rm m}, \cdot) + \eta p_{\rm m}^{(1)}(\boldsymbol{r}_{\rm m}, \cdot) + \cdots.$$

Recalling that $x = \eta x_{\rm m}$ and expanding the macroscopic fields in Taylor series near $x = 0^\pm$ for small η, we obtain

$$p^{(0)}(0^\pm, \cdot) = \lim_{x_{\rm m} \to \pm\infty} p_{\rm m}^{(0)}(\boldsymbol{r}_{\rm m}, \cdot),$$

$$p^{(1)}(0^\pm, \cdot) = \lim_{x_{\rm m} \to \pm\infty} \left(p_{\rm m}^{(1)}(\boldsymbol{r}_{\rm m}, \cdot) - x_{\rm m} \frac{\partial p^{(0)}}{\partial x}(0^\pm, \cdot) \right), \tag{26}$$

and analogous relations hold for the velocity, where $p^{(n)}$ is replaced by $\boldsymbol{u}^{(n)}$ and $p_{\rm m}^{(n)}$ is replaced by $\boldsymbol{u}_{\rm m}^{(n)}$ for $n = 0, 1$.

Jumps at order 0 – We begin by determining the order-zero transmission conditions for pressure and velocity at $x = 0^\pm$ starting from the mesoscopic problem. From Eq. (20a), it follows that $p_{\rm m}^{(0)}$ does not depend on $\boldsymbol{r}_{\rm m}$. Using the matching condition [Eq. (26)], we deduce that $p^{(0)}$ is continuous across $x = 0$, namely,

$$[\![p^{(0)}]\!] = 0, \quad p_{\rm m}^{(0)} = p^{(0)}(0, \boldsymbol{r}_\parallel, t) = P^{(0)}(\boldsymbol{r}_\parallel, t), \tag{27}$$

where $P^{(0)}(\boldsymbol{r}_\parallel, t)$ denotes the well-defined (unambiguous) value of the macroscopic pressure field at $x = 0$. Next, integrating the divergence equation $\mathrm{div}_{\rm m} \boldsymbol{u}_{\rm m}^{(0)} = 0$ in Eq. (20b) over $\Omega_{\rm m} \backslash \mathcal{B}_{\rm m}$, where $\mathcal{B}_{\rm m}$ is a sphere of vanishing radius $b_{\rm m}$ centered at $\boldsymbol{r}_{\rm m} = \boldsymbol{0}$, and taking into account the singular behavior [Eq. (21)] near the origin together with the matching condition [Eq. (26)] on $\boldsymbol{u}_{\rm m}^{(0)}$, we pass to the limit $b_{\rm m} \to 0$ and obtain a relation between the velocity jump and the amplitude of the mesoscopic singularity such that

$$[\![u_x^{(0)}]\!] = \Phi^{(0)}(\boldsymbol{r}_\parallel, t). \tag{28}$$

At this stage, $\Phi^{(0)}(\boldsymbol{r}_\parallel, t)$ remains an unknown field, whose determination requires coupling the mesoscopic and microscopic scale.

Jumps at order 1 – Using Eq. (28), the velocity at $x = 0$ can be decomposed as

$$\boldsymbol{u}^{(0)}(0^\pm, \cdot) = \left(U_x^{(0)}(\cdot) \pm \frac{1}{2} \Phi^{(0)}(\cdot) \right) \boldsymbol{e}_x + \boldsymbol{u}_\parallel^{(0)}(\cdot),$$

where $U_x^{(0)}(\boldsymbol{r}_\parallel, t) = 1/2(u_x^{(0)}(0^+, \cdot) + u_x^{(0)}(0^-, \cdot))$ is the average normal velocity across $x = 0$, and $\boldsymbol{u}_\parallel^{(0)}(\boldsymbol{r}_\parallel, t)$ is the tangential velocity component $[\boldsymbol{u}_\parallel^{(0)} \cdot \boldsymbol{e}_x = 0]$. In particular, from the first equation of Eq. (18), we obtain

$$\frac{\partial}{\partial t} \left(U_x^{(0)}(\cdot) \pm \frac{1}{2} \Phi^{(0)}(\cdot) \right) = -\frac{\partial p^{(0)}}{\partial x}(0^\pm, \cdot),$$
$$\frac{\partial \boldsymbol{u}_\parallel^{(0)}}{\partial t}(0, \cdot) = -\boldsymbol{\nabla}_\parallel P^{(0)}(\cdot), \tag{29}$$

where we have used the continuity of $p^{(0)}$ across $x = 0$ from Eq. (27). Consequently, the problem [Eq. (20b)] set on $(\boldsymbol{u}_{\rm m}^{(0)}, p_{\rm m}^{(1)})$, together with the matching condition [Eq. (26)] applied to $\boldsymbol{u}_{\rm m}^{(0)}$ as $x_{\rm m} \to \pm\infty$ and the near-origin singular behavior of $\boldsymbol{u}_{\rm m}^{(0)}$ in Eq. (21), can be reformulated as the following auxiliary problem set on $(\boldsymbol{v}_{\rm m}^{(0)}, p_{\rm m}^{(1)})$:

$$\begin{cases} \mathrm{div}_{\rm m} \boldsymbol{v}_{\rm m}^{(0)} = 0, \quad \boldsymbol{v}_{\rm m}^{(0)} = -\boldsymbol{\nabla}_{\rm m} p_{\rm m}^{(1)} \ \text{ in } \Omega_{\rm m}, \\ \boldsymbol{v}_{\rm m}^{(0)} \underset{r_{\rm m} \to 0}{\sim} \dfrac{\partial \Phi^{(0)}}{\partial t} \dfrac{\boldsymbol{e}_r}{4\pi r_{\rm m}^2}, \\ p_{\rm m}^{(1)} \text{ periodic}, \ \boldsymbol{v}_{\rm m}^{(0)} \cdot \boldsymbol{n} \text{ anti-periodic on } \partial\Omega_{\rm m}, \\ \lim\limits_{x_{\rm m} \to \pm\infty} \boldsymbol{v}_{\rm m}^{(0)} = \left(\dfrac{\partial U_x^{(0)}}{\partial t} \pm \dfrac{1}{2} \dfrac{\partial \Phi^{(0)}}{\partial t} \right) \boldsymbol{e}_x, \end{cases} \tag{30}$$

where $\boldsymbol{v}_{\rm m}^{(0)} = \partial_t(\boldsymbol{u}_{\rm m}^{(0)} - \boldsymbol{u}_\parallel^{(0)})$. Because Eq. (30) is linear with respect to the fields $\partial_t \Phi^{(0)}$ and $\partial_t U_x^{(0)}$, the general solution can be written as

$$p_{\rm m}^{(1)}(\boldsymbol{r}_{\rm m}, \cdot) = P^{(1)}(\cdot) - x_{\rm m} \frac{\partial U_x^{(0)}}{\partial t}(\cdot) - \frac{\partial \Phi^{(0)}}{\partial t}(\cdot) G_{\rm L}(\boldsymbol{r}_{\rm m}), \tag{31}$$

where $G_{\rm L}$ is the Green function defined in Eq. (7). In this definition, the Neumann boundary conditions on $\partial\Omega_{\rm m}$ are equivalent to periodic boundary conditions, owing to the symmetry of $G_{\rm L}$ with respect to $y_{\rm m}$ and $z_{\rm m}$. From the far-field behavior of $G_{\rm L}$, Eq. (31) yields

$$P^{(1)}(\cdot) = \lim_{x_{\rm m} \to \pm\infty} \left[p_{\rm m}^{(1)}(\boldsymbol{r}_{\rm m}, \cdot) + \frac{\partial}{\partial t} \left(U_x^{(0)}(\cdot) \pm \frac{1}{2} \Phi^{(0)}(\cdot) \right) x_{\rm m} \right],$$

which, combined with the first relation in Eq. (29) and the matching relation [Eq. (26)] for $p^{(1)}$, leads to the order-one continuity condition on pressure

$$[\![p^{(1)}]\!] = 0, \quad p^{(1)}(0, \boldsymbol{r}_\parallel, t) = P^{(1)}(\boldsymbol{r}_\parallel, t). \tag{32}$$

https://doi.org/10.1121/10.0041877

The jump of $u_x^{(1)}$ is obtained by integrating the second equation of Eq. (20b), as was performed previously for $u_x^{(0)}$. To that end, we need to determine $\boldsymbol{u}_{\mathrm{m}}^{(0)}(\boldsymbol{r}_{\mathrm{m}},\cdot)$ explicitly from the second equation of Eq. (20a). Using the second equation of Eq. (29) together with Eq. (31), we obtain

$$\boldsymbol{u}_{\mathrm{m}}^{(0)}(\boldsymbol{r}_{\mathrm{m}},\cdot)=\boldsymbol{u}_{\parallel}^{(0)}(\cdot)+U_x^{(0)}(\cdot)\ \boldsymbol{e}_x-\Phi^{(0)}(\cdot)\boldsymbol{\nabla}_{\mathrm{m}}G_{\mathrm{L}}(\boldsymbol{r}_{\mathrm{m}}).$$

Applying the operator $\mathrm{div}_{\parallel}$ to the above expression and substituting the result into Eq. (20b) yields

$$\mathrm{div}_{\mathrm{m}}\boldsymbol{u}_{\mathrm{m}}^{(1)}-\frac{\partial u_x^{(0)}}{\partial x}(0,\cdot)-\boldsymbol{\nabla}_{\parallel}\Phi^{(0)}\cdot\boldsymbol{\nabla}_{\mathrm{m}}G_{\mathrm{L}}=0, \tag{33}$$

where we have used the relation $-\partial_x u_x^{(0)}/\partial x(0,\cdot)=\mathrm{div}_{\parallel}\boldsymbol{u}_{\parallel}^{(0)}(0,\cdot)+\partial_t p^{(0)}(0,\cdot)$ from Eq. (18).

We now integrate Eq. (33) over $\Omega_{\mathrm{m}}\setminus\mathcal{B}_{\mathrm{m}}$, where $\mathcal{B}_{\mathrm{m}}$ is a sphere of vanishing radius b_{m} centered at $\boldsymbol{r}_{\mathrm{m}}=\boldsymbol{0}$. The contribution of the last term in Eq. (33) vanishes because $\int_{\Omega_{\mathrm{m}}}\boldsymbol{e}_a\cdot\boldsymbol{\nabla}_{\mathrm{m}}G_{\mathrm{L}}\,\mathrm{d}\boldsymbol{r}_{\mathrm{m}}=0$ for $a=y,z$, as a result of the even symmetry of G_{L} in $(y_{\mathrm{m}},z_{\mathrm{m}})$. Applying the divergence theorem to the first term and using the singular behavior given by Eq. (21) at the origin—in particular, that the integral of the r_{m}^{-3} term vanishes [see the remark following Eq. (21)]—together with the matching condition [Eq. (26)] written for u_x at order one in the limit $b_{\mathrm{m}}\to 0$, we obtain

$$[\![u_x^{(1)}]\!]=\Phi^{(1)}(\boldsymbol{r}_{\parallel},t). \tag{34}$$

As in the leading-order case, $\Phi^{(1)}(\boldsymbol{r}_{\parallel},t)$ remains an unknown field that will be determined in Sec. III C by coupling the mesoscopic and microscopic scales.

C. The connection between the meso- and micro-scales

To identify the unknown fields $(\Phi^{(0)},\Phi^{(1)})$ in Eqs. (28) and (34), we must transfer information from microscopic scale, i.e., the scale of the individual bubbles, up to the mesoscopic level. As before, this is achieved by matching the meso-scale expansions [Eq. (19)] with the micro-scale expansions [Eq. (22)] in an intermediate region where $r_{\mathrm{m}}\to 0$ and $r_\mu=|\boldsymbol{r}_\mu|\to+\infty$. For the velocity, the matching conditions read

$$\begin{aligned}&\boldsymbol{u}_{\mathrm{m}}^{(0)}(\boldsymbol{r}_{\mathrm{m}},\cdot)+\eta\boldsymbol{u}_{\mathrm{m}}^{(1)}(\boldsymbol{r}_{\mathrm{m}},\cdot)+\cdots\\ &\underset{\substack{r_{\mathrm{m}}\to 0\\ r_\mu\to+\infty}}{\sim}\frac{1}{\eta^2}\left(\boldsymbol{u}_\mu^{(0)}(\boldsymbol{r}_\mu,\cdot)+\eta\boldsymbol{u}_\mu^{(1)}(\boldsymbol{r}_\mu,\cdot)+\cdots\right),\end{aligned}$$

which, combined with the singular behavior of $\boldsymbol{u}_{\mathrm{m}}^{(n)}$, $n=0,1$, at the origin given by Eq. (21) and the change of variable $\boldsymbol{r}_{\mathrm{m}}=\ell\eta\boldsymbol{r}_\mu$, imposes the following behavior at infinity of $\boldsymbol{u}_\mu^{(n)}$:

$$\boldsymbol{u}_\mu^{(n)}(\boldsymbol{r}_\mu,\cdot)\underset{r_\mu\to+\infty}{\sim}\Phi^{(n)}(\cdot)\,\frac{\boldsymbol{e}_r}{4\pi\ell^2 r_\mu^2},\quad n=0,1. \tag{35}$$

Elementary problem at order $n=0,1$—From the first equation in Eq. (23), we deduce that for $n=0,1$, the pressures $\widetilde{p}_\mu^{(n)}$ in the bubble $\Omega_\mu^{\mathrm{gas}}$ do not depend on $\boldsymbol{r}_\mu$ and take the form

$$\widetilde{p}_\mu^{(n)}=p_r^{(n)}(\boldsymbol{r}_{\parallel},t),\qquad n=0,1, \tag{36}$$

where the pressures $p_r^{(n)}$ are yet unknown. In the liquid region $\Omega_\mu^{\mathrm{liq}}$, the fields $(\boldsymbol{u}_\mu^{(n)},p_\mu^{(n)})$, for $n=0,1$, satisfy the governing equations [Eq. (24)], subject to the continuity condition [Eq. (25)] with the bubble pressure [given in Eq. (36)] and the far-field condition [Eq. (35)]. The resulting problem is

$$\begin{cases}\mathrm{div}_\mu\boldsymbol{u}_\mu^{(n)}=0,\quad \dfrac{\partial\boldsymbol{u}_\mu^{(n)}}{\partial t}=-\dfrac{1}{\ell}\boldsymbol{\nabla}_\mu p_\mu^{(n)} & \text{in } \Omega_\mu^{\mathrm{liq}},\\ p_\mu^{(n)}(\boldsymbol{r}_\mu,\cdot)=p_r^{(n)}(\cdot) & \text{on } \partial\Omega_\mu^{\mathrm{gas}},\\ \boldsymbol{u}_\mu^{(n)}(\boldsymbol{r}_\mu,\cdot)\underset{r_\mu\to+\infty}{\sim}\Phi^{(n)}(\cdot)\,\dfrac{\boldsymbol{e}_r}{4\pi\ell^2 r_\mu^2}.\end{cases}$$

Because this problem is linear in the macroscopic quantities $p_r^{(n)}(\boldsymbol{r}_{\parallel},t)$ and $\partial_t\Phi^{(n)}(\boldsymbol{r}_{\parallel},t)$, the general solution can be written as

$$p_\mu^{(n)}(\boldsymbol{r}_\mu,\cdot)=-\frac{1}{\ell}\frac{\partial\Phi^{(n)}}{\partial t}(\cdot)G_\circ(\boldsymbol{r}_\mu)+p_r^{(n)}(\cdot), \tag{37}$$

where $G_\circ(\boldsymbol{r}_\mu)$ is the fundamental solution of the capacitance problem defined in Eq. (9), independent of macroscopic variables.

We shall now establish the following result:

$$\begin{aligned}\frac{\partial\Phi^{(0)}}{\partial t}&=\ell\Gamma_\circ\left(p_r^{(0)}-P^{(0)}\right),\\ \frac{\partial\Phi^{(1)}}{\partial t}&=\ell\Gamma_\circ\left(p_r^{(1)}-P^{(1)}+\Gamma_{\mathrm{L}}\frac{\partial\Phi^{(0)}}{\partial t}\right),\end{aligned} \tag{38}$$

where $\Gamma_\circ$ is the bubble capacitance [Eq. (10)] and Γ_{L} is the lattice parameter [Eq. (8)]. To do so, we match the microscopic and mesoscopic pressures as we did for the velocities, namely,

$$\begin{aligned}&p_\mu^{(0)}(\boldsymbol{r}_\mu,\cdot)+\eta p_\mu^{(1)}(\boldsymbol{r}_\mu,\cdot)+\cdots\\ &\underset{\substack{r_{\mathrm{m}}\to 0\\ r_\mu\to+\infty}}{\sim}p_{\mathrm{m}}^{(0)}(\boldsymbol{r}_{\mathrm{m}},\cdot)+\eta p_{\mathrm{m}}^{(1)}(\boldsymbol{r}_{\mathrm{m}},\cdot)+\eta^2 p_{\mathrm{m}}^{(2)}(\boldsymbol{r}_{\mathrm{m}},\cdot)+\cdots.\end{aligned} \tag{39}$$

Using $p_{\mathrm{m}}^{(0)}$ from Eq. (27) and $p_{\mathrm{m}}^{(1)}$ from Eq. (31) together with Eq. (7) and $\boldsymbol{r}_{\mathrm{m}}=\ell\eta\boldsymbol{r}_\mu$, yields the asymptotic behavior near the mesoscopic origin

$$\begin{aligned}&p_{\mathrm{m}}^{(0)}(\ell\eta\boldsymbol{r}_\mu,\cdot)+\eta p_{\mathrm{m}}^{(1)}(\ell\eta\boldsymbol{r}_\mu,\cdot)+\eta^2 p_{\mathrm{m}}^{(2)}(\boldsymbol{r}_{\mathrm{m}},\cdot)+\cdots\\ &\underset{\eta\to 0}{\sim}P^{(0)}(\cdot)+\frac{\partial\Phi^{(0)}}{\partial t}(\cdot)\frac{1}{4\pi\ell r_\mu}+\eta\left(P^{(1)}(\cdot)\right.\\ &\left.-\Gamma_{\mathrm{L}}\frac{\partial\Phi^{(0)}}{\partial t}(\cdot)+\frac{\partial\Phi^{(1)}}{\partial t}(\cdot)\frac{1}{4\pi\ell r_\mu}\right)+\cdots,\end{aligned}$$

where the term $\partial_t\Phi^{(1)}(1/4\pi\ell r_\mu)$ originates from the singular behavior of $p_{\rm m}^{(2)}(\boldsymbol{r}_{\rm m},\cdot)$ associated with the order-1 singular velocity term in Eq. (21) through the equation $\partial_t \boldsymbol{u}_{\rm m}^{(1)} = -\boldsymbol{\nabla}_\parallel p_{\rm m}^{(1)} - \boldsymbol{\nabla}_{\rm m} p_{\rm m}^{(2)}$ [which corresponds to Eq. (20a) pushed at the next order]. Coming back to Eq. (39), we deduce the following behavior at infinity for $(p_\mu^{(0)}, p_\mu^{(1)})$:

$$p_\mu^{(0)}(\boldsymbol{r}_\mu,\cdot) \underset{r_\mu\to+\infty}{\sim} P^{(0)}(\cdot) + \frac{\partial\Phi^{(0)}}{\partial t}(\cdot)\frac{1}{4\pi\ell r_\mu},$$
$$p_\mu^{(1)}(\boldsymbol{r}_\mu,\cdot) \underset{r_\mu\to+\infty}{\sim} P^{(1)}(\cdot) - \Gamma_{\rm L}\frac{\partial\Phi^{(0)}}{\partial t}(\cdot) + \frac{\partial\Phi^{(1)}}{\partial t}(\cdot)\frac{1}{4\pi\ell r_\mu}.$$

For $n = 0, 1$, it then suffices to combine the above equations with Eq. (37), as $r_\mu \to +\infty$, using the asymptotic behavior of $G_\circ$ at infinity given in Eq. (10) to obtain the result announced in Eq. (38).

Finally, to derive the resonator equation that governs the pressures $p_\mu^{(n)}$ for $n = 0,1$, we integrate the compressibility equation in Eq. (23) over the domain $\Omega_\mu^{\rm gas}$ and the incompressibility condition in Eq. (24) over the domain $\Omega_\mu^{\rm liq} \cap \mathcal{B}_\mu$, where $\mathcal{B}_\mu$ is the sphere centered at $\boldsymbol{r}_\mu = 0$ with sufficiently large radius b_μ to fully contain the bubble. Making use of the continuity conditions [Eq. (25)] at the interface between the two media, the fact that the pressure in the bubble is spatially uniform [see Eq. (36)] and the velocity behavior at infinity is given by Eq. (35), we obtain, upon taking the limit as $b_\mu \to +\infty$,

$$\frac{\Phi^{(n)}}{\ell^2} = \lim_{b_\mu\to+\infty}\int_{\partial\mathcal{B}_\mu} \boldsymbol{u}_\mu^{(n)}\cdot\boldsymbol{e}_r = -\ell\beta\frac{\partial p_r^{(n)}}{\partial t}, \quad n = 0, 1, \tag{40}$$

where we have accounted for a unitary bubble volume $|\Omega_\mu^{\rm gas}| = 1$. Taking the derivative with respect to time t of Eq. (40) and combining it with Eq. (38), we obtain

$$\begin{cases} \dfrac{\partial^2 p_r^{(0)}}{\partial t^2} + \dfrac{\Gamma_\circ}{\ell^2\beta}\left(p_r^{(0)} - P^{(0)}\right) = 0, \\ \dfrac{\partial^2 p_r^{(1)}}{\partial t^2} - \ell\Gamma_\circ\Gamma_{\rm L}\dfrac{\partial^2 p_r^{(0)}}{\partial t^2} + \dfrac{\Gamma_\circ}{\ell^2\beta}\left(p_r^{(1)} - P^{(1)}\right) = 0. \end{cases} \tag{41}$$

Eventually, a unique macroscopic formulation for the homogenized fields $(\overline{p}, p_r, \overline{\boldsymbol{u}})$ is obtained by expanding

$$\begin{cases} \overline{p}(\boldsymbol{r},t) = p^{(0)}(\boldsymbol{r},t) + \eta p^{(1)}(\boldsymbol{r},t) + O(\eta^2), \\ p_r(\boldsymbol{r}_\parallel,t) = p_r^{(0)}(\boldsymbol{r}_\parallel,t) + \eta p_r^{(1)}(\boldsymbol{r}_\parallel,t) + O(\eta^2), \\ \overline{\boldsymbol{u}}(\boldsymbol{r},t) = \boldsymbol{u}^{(0)}(\boldsymbol{r},t) + \eta\boldsymbol{u}^{(1)}(\boldsymbol{r},t) + O(\eta^2). \end{cases} \tag{42}$$

The leading-order equations [Eq. (18)] yield

$$\frac{\partial\overline{\boldsymbol{u}}}{\partial t} = -\boldsymbol{\nabla}\overline{p}, \quad \mathrm{div}\,\overline{\boldsymbol{u}} + \frac{\partial\overline{p}}{\partial t} = 0. \tag{43}$$

For the pressure and velocity fields, the jump conditions follow by aggregating the contributions from Eqs. (27)–(32) and (28)–(34), respectively, and by using Eq. (40) such that

$$\overline{p}(0^\pm, \boldsymbol{r}_\parallel, t) = \overline{p}(0, \boldsymbol{r}_\parallel, t),$$
$$\overline{u}_x(0^+, \boldsymbol{r}_\parallel, t) - \overline{u}_x(0^-, \boldsymbol{r}_\parallel, t) = -\ell^3\beta\frac{\partial p_r}{\partial t}(\boldsymbol{r}_\parallel, t). \tag{44}$$

The resonator equation, governing the evolution of p_r, is obtained by summing the two relations in Eq. (41),

$$(1 - \eta\ell\Gamma_\circ\Gamma_{\rm L})\frac{\partial^2 p_r}{\partial t^2}(\boldsymbol{r}_\parallel, t) + \frac{\Gamma_\circ}{\ell^2\beta}(p_r(\boldsymbol{r}_\parallel, t) - \overline{p}(0, \boldsymbol{r}_\parallel, t)) = 0. \tag{45}$$

By construction, this effective model is accurate up to second order in η. Applying the dimensional scalings introduced in Eq. (15) leads to the final macroscopic equations stated in Eqs. (5) and (6).

IV. SCATTERING BEHAVIOR OF BUBBLE SCREENS

In this section, we consider the following physical properties for the liquid and gas phases, corresponding, respectively, to water and air: $\rho_\ell = 10^3\,\mathrm{kg\cdot m^{-3}}$, $c_\ell = 1500\,\mathrm{m\cdot s^{-1}}$ for water, and $\rho_g = 1.2\,\mathrm{kg\cdot m^{-3}}$, and $c_g = 343\,\mathrm{m\cdot s^{-1}}$ for air.

A. Scattering coefficients and bubble pressure

We consider an incident plane wave of frequency ω, impinging on the bubble screen at an oblique angle (θ, φ). Although the direct problem [Eq. (3)] must be solved numerically, the homogenized model [Eqs. (4) and (5)] admits an explicit analytical solution of the form

$$\overline{p}(x, \boldsymbol{r}_\parallel, t) = e^{-i\omega t + \boldsymbol{k}_\parallel\cdot\boldsymbol{r}_\parallel}\begin{cases} e^{ik_x x} + Re^{-ik_x x} & \text{for } x < 0, \\ Te^{ik_x x} & \text{for } x > 0, \end{cases} \tag{46}$$

where (R, T) are the homogenized reflection and transmission coefficients; $k_x = k\cos\theta$, $\boldsymbol{k}_\parallel = k\sin\theta(\cos\varphi\,\boldsymbol{e}_y + \sin\varphi\,\boldsymbol{e}_z)$, where $k = \omega/c_\ell$ is the wavenumber in water. At $x = 0$, the homogenized bubble pressure p_r, governed by the resonator equation in Eq. (5) [or, equivalently, Eq. (13)], also takes the form of a plane wave propagating in the (y, z)-plane such that

$$p_r(x, \boldsymbol{r}_\parallel, t) = P_r\; e^{-i\omega t + \boldsymbol{k}_\parallel\cdot\boldsymbol{r}_\parallel}. \tag{47}$$

The coefficients (R, T, P_r) are determined from Eqs. (4) and (5). A direct calculation yields

$$R = \frac{i\kappa_x d}{(\omega_r^\infty/\omega)^2 - 1 + \Gamma_\circ\Gamma_{\rm L}d/h - i\kappa_x d}, \quad T = 1 + R,$$
$$P_r = \frac{(\omega_r^\infty/\omega)^2}{(\omega_r^\infty/\omega)^2 - 1 + \Gamma_\circ\Gamma_{\rm L}d/h - i\kappa_x d}, \tag{48}$$

where

https://doi.org/10.1121/10.0041877

$$\kappa_x = \frac{\Gamma_\circ}{2k_x h^2}, \tag{49}$$

and parameters $(\omega_r^\infty, \Gamma_\circ, \Gamma_{\rm L})$ are defined in Eqs. (2), (8), and (10), respectively. These expressions generalize earlier results obtained for square lattices with spherical bubbles by accounting for arbitrary incidence angles, bubble shape, and lattice configurations. In particular, comparison with the well-established model of Leroy *et al.* (2009) is provided in Appendix B. An equivalent but more conventional form of these coefficients, involving only (ω_r, Q) defined in Eqs. (6) and (14), is given by

$$\begin{aligned} R &= \frac{2i\Omega/Q}{1-\Omega^2-2i\Omega/Q}, \quad T = 1+R, \\ P_r &= \frac{1}{1-\Omega^2-2i\Omega/Q}, \end{aligned} \tag{50}$$

where $\Omega = \omega/\omega_r$ (see Lanoy *et al.*, 2018, in the context of bubble screens).

In the following, these scattering coefficients associated with the homogenized solution [Eq. (46)] are compared with results from direct numerical simulations. The latter are obtained by solving the full-scale problem defined by the Euler equations [Eq. (3)] together with the usual continuity conditions at the air–water interface, using the Acoustics Module of COMSOL Multiphysics (COMSOL AB, Stockholm, Sweden). The computations are performed in a three-dimensional rectangular domain consisting of the (y,z) plane, a single elementary cell of dimensions (h_y, h_z) and surface area $S = h_y h_z$, and extending over a length $2L_x \sim 10h$ along the $x-$ direction $(h = \sqrt{S})$. The domain contains a single bubble, resulting in approximately 10^6 degrees of freedom. Bloch–Floquet boundary conditions are imposed on the lateral faces of the domain $(y = \pm h_y/2$ and $z = \pm h_z/2)$, whereas perfectly matched layers are applied at $x = \pm L_x$. The incident plane wave is introduced through the background pressure field feature.

To begin with, the validity of the model is illustrated in Fig. 3, which shows the pressure field in the plane $z = 0$ for a bubble screen composed of spherical bubbles of radius $a = 50\,\mu$m arranged in a square lattice with $h = 40a$. The incident wave at $f = 83$ kHz, slightly above the resonance frequency at $\omega_r/2\pi \simeq 69$ kHz, impinges on the bubble screen at an angle of $\theta = 45°$ with $\varphi = 0°$. The qualitative agreement is good, demonstrating the ability of the homogenized model to reproduce the far-field pattern.

In Secs. IV B–IV D, we validate the model more quantitatively. We will examine the effects of bubble density and shape as well as the effects of the lattice arrangement. To simplify the comparison, we will consider bubbles of the same volume $V = 4\pi a^3/3$, where $a = 50\,\mu$m, and the reference case is spherical bubbles of radius a.

B. Effect of the bubble density

We begin by examining the effect of bubble size to periodicity ratio a/h, which measures the bubble density in the screen. We focus on spherical bubbles in a square lattice,

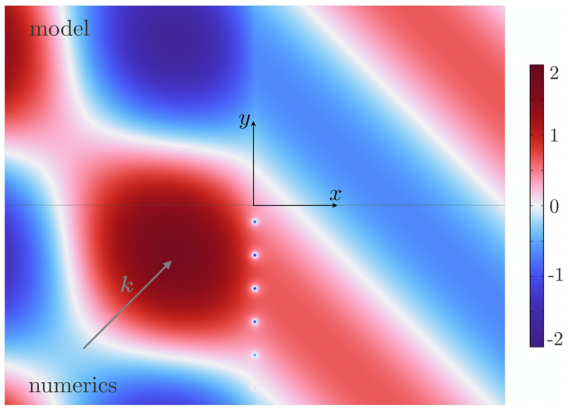

FIG. 3. Illustration of the model accuracy. Real part of the pressure field in the plane $z = 0$ for a bubble screen composed of spherical bubbles in a square lattice ($a = 50\,\mu$m, $h = 200\,\mu$m) is shown. The incident wave propagates at 45° to the x axis with $\varphi = 0$ and a frequency of 83 kHz. The comparison is performed by showing, for $y > 0$, the analytical solution of the homogenized model, Eqs. (46)–(48), and for $y < 0$, the field obtained from direct numerical simulations (where the bubble array is explicitly resolved) is depicted. In the direct numerical calculation, we used $L_x = 3000\,\mu$m. The field displayed for $y < 0$ has been constructed by extending the numerical solution along the y direction using Bloch–Floquet periodicity.

which occupy a central place in the literature. For a bubble of radius a, the characteristic length d is given by

$$d = \left(\frac{4\pi}{3}\right)^{1/3} a. \tag{51}$$

Next, the parameters take the form

$$\begin{aligned} \Gamma_\circ &= \Gamma_\circ^{\rm sph} = 4\pi\left(\frac{4\pi}{3}\right)^{-1/3} \quad \text{(spherical bubble)}, \\ \Gamma_{\rm L} &= \Gamma_{\rm L}^{\rm sq} \simeq \frac{3.9}{4\pi} \quad \text{(square lattice)}. \end{aligned} \tag{52}$$

In particular $\Gamma_\circ^{\rm sph} d = 4\pi a$ is the usual, dimensional capacitance of a sphere (see Appendix A 1).

The value of $\Gamma_\circ^{\rm sph}$ is exact because for a spherical bubble, the capacitance problem [Eq. (9)] admits the closed-form solution $G_\circ = 1/4\pi a_\mu - 1/4\pi r_\mu$, where $a_\mu = (3/4\pi)^{1/3}$ is the radius of a unit-volume bubble. The value of $\Gamma_{\rm L}$ was calculated in Pham *et al.* (2021b), using the explicit series representation of the Green function $G_{\rm L}$ in Eq. (7) [see Eqs. (2.9), (2.10), and related text in Pham *et al.*, 2021b].

Using Eq. (52) in Eq. (2), we recover the Minnaert frequency for a single (spherical) bubble such that

$$\omega_r^\infty = \frac{c_g}{a}\sqrt{3\frac{\rho_g}{\rho_\ell}}, \tag{53}$$

as expected. This same frequency is also recovered from Eq. (6) in the infinitely dilute limit $d/h \to 0$. The frequency shift resulting from collective effects of bubbles in the array is given by the shifting parameter $\Gamma_{\rm L}\Gamma_\circ d/h = 3.9\ a/h$, which is in good agreement with the prediction reported in Leroy *et al.* (2009) based on physical arguments.

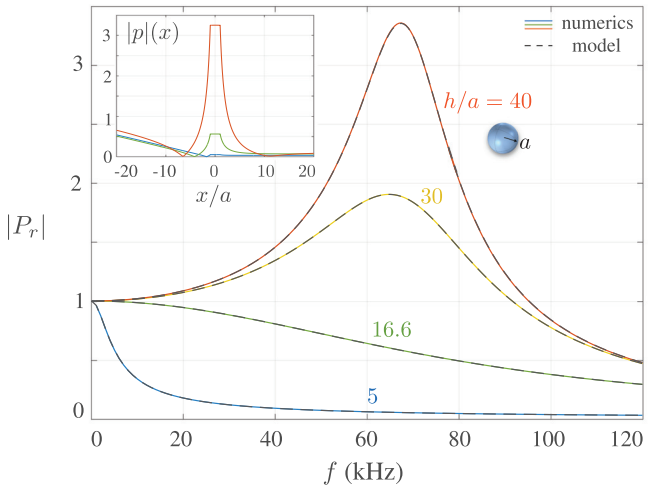

FIG. 4. Spherical bubbles in a square lattice. Pressure amplitude against frequency with varying bubble density $h/a = (40, 30, 16.6, 5)$ for constant $a = 50$ μm is depicted. Solid lines show numerical results, and dashed black lines respresent the results from the model [Eq. (48)] [or equivalently Eq. (50)] The inset shows the numerically obtained pressure amplitude along x covering the regions outside and inside a single bubble at $f = 70$ kHz.

To assess the influence of bubble density in the array, we consider bubbles of radius $a = 50$ μm arranged in the lattice with four different periodicities: $h = (40, 30, 16.6, 5)a$. A normally incident wave in the frequency range f between 0 and 120 kHz is considered. Figures 4 and 5 show, respectively, the bubble pressure amplitude $|P_r|$ and the reflection coefficient R as functions of frequency, with solid lines from numerical simulations and black dashed lines from the model [Eq. (48)] [or equivalently Eq. (50); see Table I]. The insets display the numerically obtained profiles of the pressure amplitude $|p|(x)$ along a line crossing the center of a bubble, confirming the uniform pressure inside the bubble, as expected and predicted by the model. The considered density range spans (i) the under-damped regime for dilute arrays ($Q > 1$ for $h/a > 16.2$), characterized by a resonant response with a strong pressure maximum

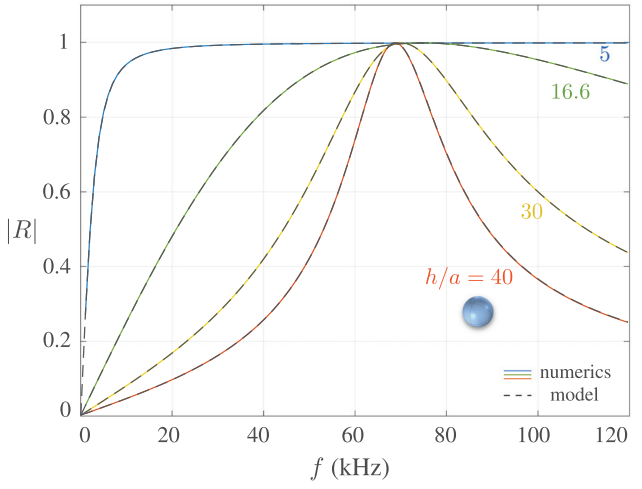

FIG. 5. Spherical bubbles in a square lattice. Reflection coefficient against frequency with varying bubble density $h/a = (40, 30, 16.6, 5)$, as in Fig. 4, is shown.

TABLE I. Spherical bubble screen in a square lattice. Resonance frequencies ω_r, Eq. (6), and quality factor Q, Eq. (14), for bubble radius $a = 50$ μm in a square lattice with $h = h_y = h_z$ are shown. Constant values are $\Gamma_\circ d = \Gamma_\circ^{\mathrm{sph}} d = 4\pi a$, $\Gamma_{\mathrm{L}} = 3.9/4\pi$, and $\omega_r^\infty/2\pi = 65.52$ kHz.

	$\omega_r/2\pi$ (kHz)	Q
$h = 40a$	68.96	6.64
$h = 30a$	70.23	3.67
$h = 16.6a$	74.89	1.05
$h = 5a$	139.66	0.05

and perfect reflection, (ii) the over-damped regime, where the bubble pressure rapidly vanishes when increasing the frequency, leading to nearly perfect reflection across the entire frequency range as a result of the highly echogenic nature of large bubbles. All of these features are accurately captured by the model, with relative errors between numerics and model remaining below 0.4% for all reported curves without visible increase with frequency.

C. Effect of bubble shape: Spheroidal and cylindrical bubbles

We now investigate how the bubble shape affects the response of the screen. To this end, we first consider a class of spheroidal bubbles with identical volume $V = (4\pi a^3/3)$, defined as

$$\frac{\mathsf{x}^2}{(e^{-2/3}a)^2} + \frac{\mathsf{y}^2 + \mathsf{z}^2}{(e^{1/3}a)^2} = 1, \tag{54}$$

where e is the eccentricity and the x axis is the axis of rotational symmetry. The spheroid is prolate if $e > 1$ and oblate if $e < 1$. The capacitance of spheroidal bubbles can be expressed in closed form such that

$$\Gamma_\circ = \Gamma_\circ^{\mathrm{sph}} g(e),$$
$$g(e) = e^{-2/3} \begin{cases} \dfrac{\sqrt{e^2-1}}{\operatorname{atan}\sqrt{e^2-1}}, & e \geq 1, \\ \dfrac{\sqrt{1-e^2}}{\operatorname{atanh}\sqrt{1-e^2}}, & e \leq 1, \end{cases} \tag{55}$$

where $g(1) = 1$ corresponds to the spherical case; see, e.g., Eqs. (24) and (31) in Spratt *et al.* (2017).

To isolate the effect of bubble shape alone, we consider a square lattice, for which $\Gamma_{\mathrm{L}} = \Gamma_{\mathrm{L}}^{\mathrm{sq}}$ is given by Eq. (52). To emphasize that the effective model depends solely on the bubble size and shape (not on its orientation), the spheroid is rotated such that $\boldsymbol{e}_{\mathsf{x}} = (\boldsymbol{e}_x + \boldsymbol{e}_z)/\sqrt{2}$.

In Fig. 6, we report the reflection coefficient as a function of frequency for $h = 40a$ (with $a = 50$ μm) and varying eccentricity $e = 1/4$, 1, and 8. According to Eq. (55) and as illustrated in the inset, the spherical bubble ($e = 1$) minimizes the capacitance $\Gamma_\circ$, which leads to the lowest resonance frequency. Deviations from spherical geometry ($e \neq 1$) result in an upward (blue) shift of the resonance frequency, accompanied by a reduction of the quality factor;

https://doi.org/10.1121/10.0041877

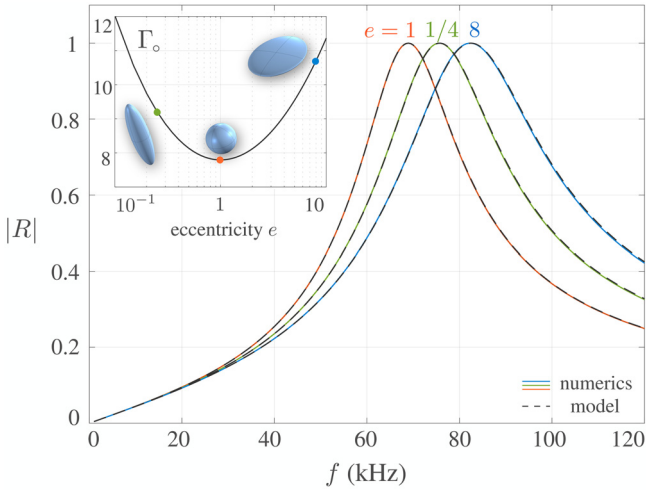

FIG. 6. Spheroidal bubbles in a square lattice. Reflection coefficients as function of frequency for eccentricity $e = 1/4$, 1, and 8 [see Eq. (54)] are shown. The bubble volume is kept constant at $V = 4\pi a^3/3$ with $a = 50$ μm, and the lattice spacing is $h = 40a$. The inset shows the variation of $\Gamma_\circ$ with eccentricity e.

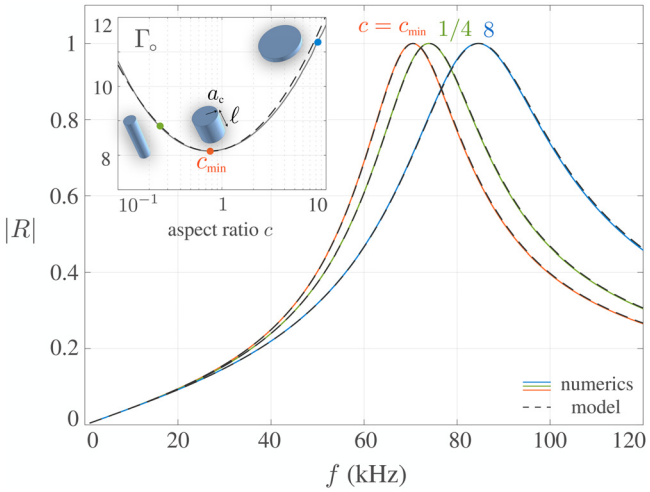

FIG. 7. Cylindrical bubbles in a square lattice. Reflection coefficients as a function of frequency for aspect ratios $c = 0.25$, 0.77, and 8 are shown. The bubble volume is $V = \pi a_c^2 \ell_c = 4\pi a^3/3$ with $a = 50$ μm, and the lattice spacing is $h = 40a$. The inset shows the capacitance $\Gamma_\circ$ versus c, obtained numerically (gray solid line) and from the estimate in Eq. (58) (black dashed line). The minimum capacitance occurs at $c_{\min} = 0.77$.

see Table II. Once again, the effective model closely matches the numerical results. The relative errors for $e \neq 1$ is slightly larger than that for $e = 1$, reaching up to 0.8%, but this can be attributable to numerical inaccuracies arising from mesh resolution.

We now turn to cylindrical bubble screens, widely studied in water-like gels because of their relative ease of fabrication. We consider cylinders of height ℓ_c and radius a_c with constant volume $V = \pi a_c^2 \ell_c = 4\pi a^3/3$. This family can be parameterized by the aspect ratio c, which is defined as

$$c = \frac{4a_c}{3\ell_c} = \left(\frac{a_c}{a}\right)^3, \tag{56}$$

such that $a_c = c^{1/3}a$ and $\ell_c = (4/3)c^{-2/3}a$. Cylindrical bubbles of equal volume are, therefore, described by

$$\frac{3x}{2c^{-2/3}a} \in (-1, 1), \quad \frac{y^2 + z^2}{(c^{1/3}a)^2} = 1. \tag{57}$$

To our knowledge, no closed-form expression for the capacitance $\Gamma_\circ$ exists for a cylinder. We computed it numerically by solving Eqs. (9) and (10) for unit-volume cylinders with aspect ratios c ranging from 0.1 to 10. A good estimate of the numerical values is

$$\Gamma_\circ = 8.12 + 0.6\left(\log \frac{c}{0.77}\right)^2, \tag{58}$$

which is illustrated in the inset of Fig. 7. The capacitance of a cylinder is always larger than that of a sphere ($\Gamma_\circ^{\text{sph}} \simeq 7.80$), with a minimum of 8.12 at $c = c_{\min} = 0.77$, corresponding to $a_c \simeq 0.9a$ and $\ell_c \simeq 1.6a$.

Figure 7 displays the reflection coefficient $|R|$ versus frequency for different aspect ratios c in the same way as in Fig. 6: a square lattice with $h = 40a$ (with $a = 50$ μmm) and $c = 1/4$, $c_{\min}$, and 8. The case $c = c_{\min}$ yields the lowest resonance frequency and the highest quality factor, which is very close—but not identical— to the spherical case for equal bubble volume (see Table III for $c = c_{\min}$ compared with spherical bubbles in Table I for $h = 40a$).

In conclusion, Figs. 6 and 7 together with Tables II and III highlight how the response of a bubble screen, made of bubbles of equal volume arranged identically in a lattice, depends on their shape. All observed variations arise from changes in the capacitance $\Gamma_\circ$, which the model reproduces accurately. Notably, the results confirm that bubbles with aspect ratios e or c close to unity behave almost like spheres—the required degree of "closeness" depending on

TABLE II. Spheroidal bubble screen. Capacitances $\Gamma_\circ$, Eq. (55), resonance frequencies ω_r^∞, Eq. (2), ω_r, Eq. (6), and quality factor Q, Eq. (14), for square lattice with $h = 40a$ of bubbles with same volume $V = d^3 = 4\pi a^3/3$, $a = 50$ μm, and eccentricities $e = 1$, 1/4, and 8 are shown.

	$\Gamma_\circ/\Gamma_\circ^{\text{sph}}$	$\omega_r^\infty/2\pi$ (kHz)	$\omega_r/2\pi$ (kHz)	Q
$e = 1/4$	1.18	71.23	75.73	6.04
$e = 1$	1	65.52	68.96	6.64
$e = 8$	1.37	76.75	82.47	5.55

TABLE III. Cylindrical bubble screen with square lattice. Same presentation as Table II, with c defined as in Eq. (56), for bubbles with identical reference volume $V = 4\pi a^3/3$ with $a = 5\ 10^{-5}$ m. $\Gamma_\circ$ is computed numerically with estimate in Eq. (58), ω_r^∞ in Eq. (2), and constant value of $d = (4\pi/3)^{1/3}a$.

	$\Gamma_\circ/\Gamma_\circ^{\text{sph}}$	$\omega_r^\infty/2\pi$ (kHz)	$\omega_r/2\pi$ (kHz)	Q
$c = 1/4$	1.14	69.80	74.01	6.18
$c = 0.77$	1.04	66.87	70.55	6.49
$c = 8$	1.44	78.52	84.68	5.41

the level of accuracy sought. It should be emphasized, however, that these effects may be significantly altered when the bubbles are embedded in a gel-like solid matrix as in underwater applications. In that case, nonspherical inclusions would excite not only pressure waves, as in the purely acoustic case, but also shear waves in the surrounding solid medium (Calvo *et al.*, 2012, 2015; Thieury *et al.*, 2020).

D. Effect of lattice arrangement

We now investigate how the lattice arrangement affects the screen's response. Previous studies have reported that collective interactions in a periodic array lead to an upward (blue) shift of the resonance frequency relative to that of an isolated bubble (Leroy *et al.*, 2009; Skvortsov *et al.*, 2019). This behavior has been consistently observed for square lattices thus far, i.e., $\omega_r^\infty < \omega_r$. To the best of our knowledge, however, the influence of the lattice arrangement has not been examined in detail and, in particular, no downward (red) shift has yet been documented. From the expression of the resonance frequency for a bubble screen [Eq. (6)], a blue shift (respectively, red shift) occurs when the lattice parameter Γ_L is positive (respectively, negative) because the capacitance parameter $\Gamma_\circ$ is always positive (see Appendix A 1).

The parameter Γ_L was computed numerically for a rectangular lattice with aspect ratio h_y/h_z by solving Eqs. (7) and (8) (see also Appendix A 2), i.e., in a cell with unitary surface. The variation of Γ_L with the aspect ratio h_y/h_z is shown in the inset of Fig. 8 and can be reasonably approximated by

$$\Gamma_L \simeq \frac{3.9}{4\pi} + \frac{0.75}{4\pi}\left(\frac{h_y}{h_z} + \frac{h_z}{h_y} - 2\right), \tag{59}$$

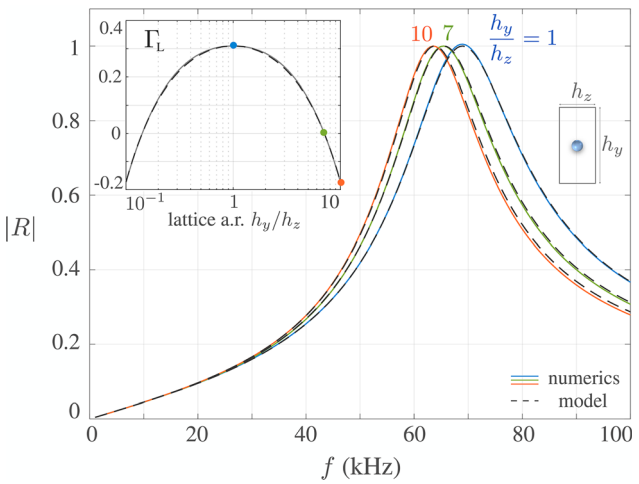

FIG. 8. Influence of the lattice arrangement. $|R|$ versus frequency for spherical bubbles ($a = 50\,\mu$m) in rectangular lattices with identical surface $S = h^2 = h_y h_z$ ($h = 200\,\mu$m) and aspect ratios $h_y/h_z = 1$, 7, and 10 is depicted. The inset shows the variation of Γ_L against h_y/h_z, computed numerically (gray solid line) and from the estimate [Eq. (58)] (black dashed line).

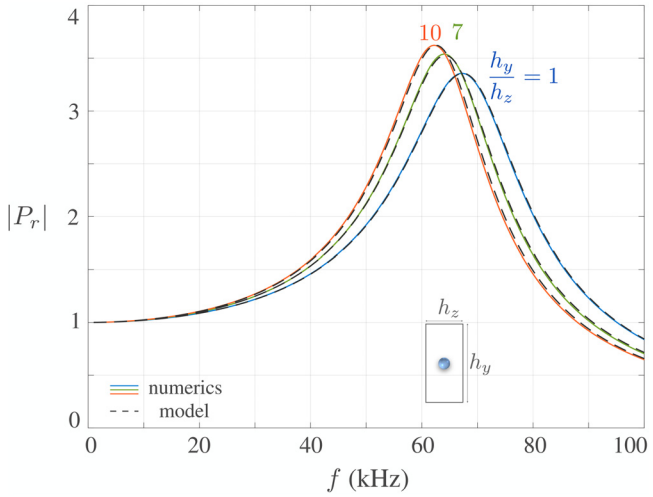

FIG. 9. Influence of the lattice arrangement. Bubble pressure amplitude versus frequency is shown for the same configuration as presented in Fig. 8.

which indicates that Γ_L turns negative when the aspect ratio exceeds approximately seven.

To confirm this red shift, we came back to spherical bubbles of radius $a = 50\,\mu$m, but now the bubbles are arranged in rectangular lattices of identical surface $S = h^2 = h_y h_z$, with $h = 40a$, and different aspect ratios, h_y/h_z was varied as 1, 7, and 10. The case $h_y/h_z = 7$ is expected to produce no frequency shift, whereas $h_y/h_z = 10$ should produce a red shift. These predictions are confirmed in the main panels of Figs. 8 and 9, which show the reflection coefficient and bubble pressure as functions of frequency. As the aspect ratio deviates from one (square lattice), the resonance frequency decreases, leading to $\omega_r \simeq \omega_r^\infty$ for $h_y/h_z = 7$, and a red shift ($\omega_r < \omega_r^\infty$) for $h_y/h_z = 10$. This frequency reduction is accompanied by an increase in the quality factor Q, as observed in Fig. 9, where the bubble pressure increases as h_y/h_z increases (see also Table IV).

To conclude this section, we note that the effective model predicts that the scattering coefficients [Eq. (48)] are independent of angle φ, which corresponds to the orientation of the incident wavevector projection in the (y, z) plane. This implies isotropic behavior in the lattice plane. Such isotropy is generally accepted for square lattices as the lattice spacing is subwavelength: in our reference case with $h = 40a$ and $a = 50\,\mu$m, the wavelength in water at

TABLE IV. Effect of the lattice arrangement. Lattice parameters Γ_L for rectangular lattices of aspect ratio $h_y/h_z = 1$, 7, and 10, normalized to $\Gamma_L^{sq} = 3.9/4\pi$ (square lattice $h_y/h_z = 1$), resonance frequencies ω_r, Eq. (6), and quality factors Q, Eq. (14), for spherical bubble of radius $a = 50\,\mu$m and $h^2 = h_y h_z = (40a)^2$ are shown. The resonance frequency of an isolated bubble is $\omega_r^\infty/2\pi = 65.52$ kHz from Eq. (6) with $\Gamma_\circ d = 4\pi a$.

	Γ_L/Γ_L^{sq}	$\omega_r/2\pi$ (kHz)	Q
$h_y/h_z = 1$	1	68.96	6.64
$h_y/h_z = 7$	0.01	65.54	6.98
$h_y/h_z = 10$	−0.56	63.79	7.18

https://doi.org/10.1121/10.0041877

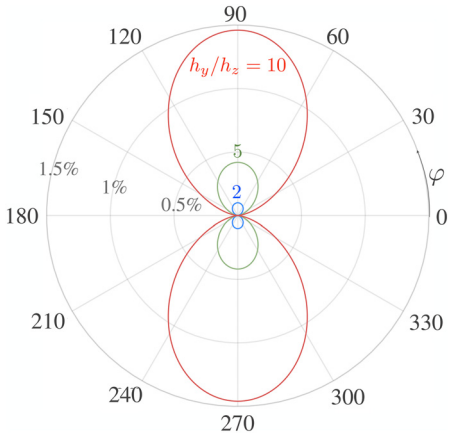

FIG. 10. Anisotropy in the response for rectangular lattice with $h_z/h_y \in (2, 5, 10)$. For nearly square lattices ($h_z/h_y = 2$), the anisotropy is negligible (of order 10^{-3}%) and magnified by a factor of 100.

resonance is about 10 times larger than h (and about 400 times larger than the bubble size a). However, for highly anisotropic rectangular lattices, such as $h_y/h_z = 10$, the wavelength is only about three times larger than the spacing in the y direction (with kh_y close to two at resonance), making isotropy in the lattice plane less certain.

To quantify this anisotropy, we performed numerical simulations for an oblique incidence at $\theta = 45^\circ$ with varying φ from 0° to 90°. Figure 10 shows the relative deviation of the numerically computed reflection coefficient from its value at $\varphi = 0$ for $h_y/h_z = 2$, 5, and 10. As expected, for nearly square lattices, the anisotropy is negligible ($\sim 10^{-3}$%, magnified by a factor of 100 in Fig. 10). As the aspect ratio increases, the angular dependence becomes more pronounced but remains small, below 2% even for $h_y/h_z = 10$. This very small anisotropy, not captured by the homogenized model, is of the same order of magnitude or smaller than the model error in the reported cases: in Figs. 8 and 9, the relative errors increase significantly with h_y/h_z, remaining below 0.4%, 1%, and 1.5% for $h_y/h_z = 1$, 7, and 10, respectively (in this case, the mesh resolution is not really concerned). For $h_y/h_z = 7$ and 10, we observe that the errors increase with frequency, which is quite expected as kh_y is no longer small.

V. CONCLUSION

In this work, we have derived a time-domain effective model for acoustic propagation through a metascreen formed by a periodic array of bubbles embedded in a liquid. The model is expressed as transmission conditions across a zero-thickness interface: the pressure remains continuous, whereas the normal velocity exhibits a jump driven by the internal gas pressure in the bubbles. This gas pressure obeys a damped mass–spring equation, unambiguously revealing the resonance frequency ω_r and quality factor Q of the bubble screen. A key outcome of this study is the identification of two geometric parameters—a capacitance-like parameter $\Gamma_\circ$, dependent on bubble shape, and a lattice parameter Γ_L, encoding the effect of the array arrangement—that fully govern the acoustic response of the screen. The framework captures the interplay between individual bubble resonances and collective effects within the array and can be applied to any bubble screen configuration, highlighting the critical role of shape and lattice configuration on the overall response.

Comparisons with direct numerical simulations confirm that the model accurately reproduces the resonant scattering behavior of the bubble screen over a broad frequency range. Its predictive capability extends across a wide variety of configurations, including different bubble shapes and volumes, lattice geometries, and angles of incidence. Two key conclusions emerge from this analysis. First, the shift in the resonance frequency of the array relative to that of an isolated bubble can be either positive (blue shift) or negative (red shift), depending on the lattice arrangement. Although a blue shift is typically observed for square arrays, the model predicts—and simulations confirm—that a red shift arises in rectangular lattices with sufficiently large aspect ratios. Second, despite that the rectangular lattices may intuitively be expected to induce anisotropic scattering, the effective model remains remarkably accurate: even for highly elongated unit cells, the angular dependence of the scattering coefficients remains weak, demonstrating that the isotropic approximation inherent to the effective model is robust and reliable.

Future investigations could address very dense bubble arrays: although their practical relevance may be limited, as the metascreen behaves essentially like a wall with vanishing bubble pressure even at low frequencies, a formal analysis relaxing the scale separation between bubble size and lattice spacing could provide insight into the transition regime between dilute and dense arrays. Extensions also concern more realistic settings. For spherical bubbles in water, additional physical effects—such as surface tension, viscosity, and thermal exchanges—in principle, may be incorporated into the resonator equation, as briefly discussed in Caflisch *et al.* (1985). For bubbles of arbitrary shape, however, practical realizations typically involve embedding the inclusions in viscoelastic matrices, which stabilize the shape but modify the surrounding medium. Incorporating such viscoelastic effects represents a promising direction for practical bubble metascreens due to their relative ease of fabrication and would allow the exploration of additional oscillation modes associated with the presence of shear waves. Finally, considering unit cells with multiple bubbles will give rise to hybridized resonances (Feuillade, 1995), opening new perspectives for achieving perfect absorption and richer wave manipulation.

ACKNOWLEDGMENTS

K.P. acknowledges the support of the Agence Natioanle de la Recherche (French National Research Agency) under Grant No. ANR-19-CE08-0006 MetaReso.

AUTHOR DECLARATIONS

Conflict of Interest

The authors have no conflicts to disclose.

DATA AVAILABILITY

The data that support the findings of this study are available from the corresponding author upon reasonable request.

APPENDIX A

1. The electrostatic capacitance

We first note that $\Gamma_\circ$ is a dimensionless parameter, whereas capacitance is usually defined as having dimension of length. We define $\Gamma_\circ$ for a bubble of arbitrary shape but with *unit volume*. For example, $C^{\rm sph} = 4\pi a$, where a is the radius of the sphere. Hence, $a = (4\pi/3)^{-1/3}$, leading to $\Gamma_\circ^{\rm sph}$ in Eq. (52). In other words, with $d = V^{1/3}$, one obtains $C = \Gamma_\circ d$.

Aside from this normalization, the normalized electrostatic capacitance $C_{\rm n} = C/d$ of a conductor occupying a region $\Omega_\mu^{\rm gas}$ and surrounded by a domain $\Omega_\mu^{\rm liq}$ is classically defined as

$$C_{\rm n} = -\int_{\partial\Omega_\mu^{\rm gas}} \boldsymbol{\nabla}_\mu V \cdot \boldsymbol{n}\, {\rm d}S, \tag{A1}$$

where $\boldsymbol{n}$ denotes the unit normal vector pointing outward from the conductor, i.e., pointing into the surrounding domain $\Omega_\mu^{\rm liq}$, and V satisfies the Laplace boundary-value problem

$$\begin{aligned} &\Delta_\mu V = 0 \ \text{ in } \Omega_\mu^{\rm liq}, \quad V = 1 \ \text{ on } \partial\Omega_\mu^{\rm gas}, \\ &\boldsymbol{\nabla}_\mu V \underset{r_\mu\to+\infty}{\sim} -\frac{C_{\rm n}}{4\pi r_\mu}\boldsymbol{e}_r \end{aligned} \tag{A2}$$

(Smythe, 1950). It is easy to verify that $C_{\rm n} = \Gamma_\circ$ and $V = 1 - \Gamma_\circ G_\circ$, where $(\Gamma_\circ, G_\circ)$ are defined in Eqs. (9) and (10).

A fundamental property of the capacitance $\Gamma_\circ$ is that it is always strictly positive. Indeed, multiplying Eq. (A2) by V and integrating by parts yields

$$\Gamma_\circ = \int_{\Omega_\mu^{\rm liq}} \boldsymbol{\nabla}_\mu V \cdot \boldsymbol{\nabla}_\mu V \, {\rm d}\Omega > 0. \tag{A3}$$

This expression shows that $\Gamma_\circ$ is strictly positive. If $\Gamma_\circ = 0$, then $\boldsymbol{\nabla}_\mu V = \boldsymbol{0}$ almost everywhere in $\Omega_\mu^{\rm liq}$, which would imply that V is constant—contradicting the boundary condition $V = 1$ on $\partial\Omega_\mu^{\rm gas}$ and the decay condition at infinity in Eq. (A2).

2. Numerical computation of $\Gamma_\circ$ and $\Gamma_{\rm L}$

The capacitance parameter $\Gamma_\circ$ defined in Eq. (9) can be computed straightforwardly using standard finite element method software. To approximate the unbounded domain, the gas bubble of unit volume is enclosed in a sphere of finite radius $R_{\rm num}$. For bubbles without extreme aspect ratios, $R_{\rm num} = 7$ suffices to capture the evanescent fields; see Fig. 11. The numerical solution $G_\circ^{\rm num}(\boldsymbol{r}_\mu)$ satisfies

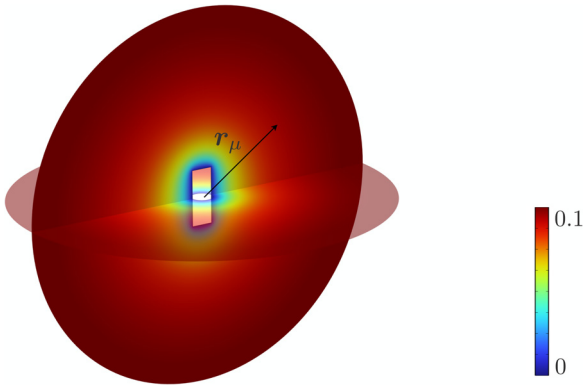

FIG. 11. Numerical $G_\circ \simeq G_\circ^{\rm num}$ for a cylindrical bubble of unitary volume with aspect ratio $c = 1/4$ [see Eq. (56)] and $R_{\rm num} = 7$.

$$\begin{cases} \Delta G_\circ^{\rm num} = 0 \ \text{ in } \Omega_\mu^{\rm liq}, \quad G_\circ^{\rm num} = 0 \ \text{ on } \partial\Omega_\mu^{\rm gas}, \\ \boldsymbol{\nabla} G_\circ^{\rm num} \cdot \boldsymbol{e}_r = \dfrac{1}{4\pi (R_{\rm num})^2} \quad \text{at } r_\mu = R_{\rm num}, \end{cases}$$

and the capacitance is numerically approximated by

$$\frac{1}{\Gamma_\circ} \simeq \frac{1}{4\pi R_{\rm num}^2} \int_{r_\mu = R_{\rm num}} \left(G_\circ^{\rm num} + \frac{1}{4\pi R_{\rm num}} \right) {\rm d}\boldsymbol{r}_\mu.$$

The lattice parameter $\Gamma_{\rm L}$ defined in Eq. (7) requires more care due to the singularity at the origin. We introduce

$$H_{\rm L}(\boldsymbol{r}_{\rm m}) = G_{\rm L}(\boldsymbol{r}_{\rm m}) + \frac{1}{4\pi r_{\rm m}},$$

which is regular at the origin and harmonic. Because the singularity of $G_{\rm L}$ is centered at the origin, $G_{\rm L}$ and $H_{\rm L}$ are even in $y_{\rm m}$ and $z_{\rm m}$. This symmetry allows periodic boundary conditions in Eq. (7) to be replaced with Neumann conditions.

The numerical implementation is performed in COMSOL Multiphysics using the weak form partial differential equation package (see Fig. 12). We consider a guide of finite length $2L_{\rm num}$ along $\boldsymbol{e}_x$, where $H_{\rm L}$ is approximated by $H_{\rm L}^{\rm num}$, satisfying the Laplace boundary-value problem

$$\begin{cases} \Delta_{\rm m} H_{\rm L}^{\rm num} = 0 \ \text{ in } \Omega_{\rm m}, \\ \boldsymbol{\nabla}_{\rm m} \left(H_{\rm L}^{\rm num} - \dfrac{1}{4\pi r_{\rm m}} \right) \cdot \boldsymbol{n} = 0 \quad \text{on } \partial\Omega_{\rm m}, \\ H_{\rm L}^{\rm num}(\pm L_{\rm num}, y_{\rm m}, z_{\rm m}) = \dfrac{L_{\rm num}}{2} + \dfrac{1}{4\pi\sqrt{L_{\rm num}^2 + y_{\rm m}^2 + z_{\rm m}^2}}. \end{cases}$$

In practice, $L_{\rm num} = 3$ is sufficient to capture the relevant evanescent fields, yielding a converged value of the approximated lattice parameter

$$\Gamma_{\rm L} \simeq H_{\rm L}^{\rm num}(\boldsymbol{0}).$$

https://doi.org/10.1121/10.0041877

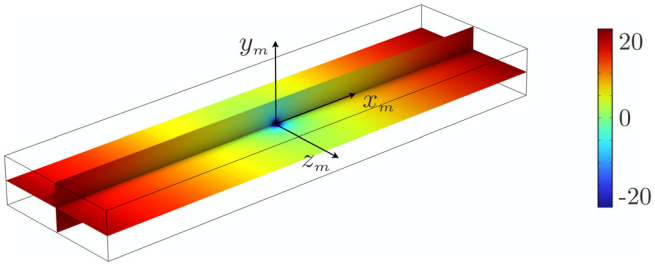

FIG. 12. Numerical Green function $G_{\mathrm{L}} \simeq H_{\mathrm{L}}^{\mathrm{num}} - 1/4\pi r_{\mathrm{m}}$ for a periodic computational domain of unitary cross-sectional area with aspect ratio $h_y/h_z = 1/3$ and $L_{\mathrm{num}} = 3$ is shown.

APPENDIX B

The most widely used model in the literature was proposed by Leroy *et al.* (2009) and describes spherical bubbles arranged in a square lattice. It takes the same form as Eq. (48), with the following notations:

$$R = \frac{iKa}{(\omega_r^\infty/\omega)^2 - I - i(Ka + \delta_{\mathrm{v}})}, \tag{B1}$$

where I is responsible for the resonance frequency shift as a result of collective effects of the bubbles, Ka is the so-called super-radiation term, and δ_{v} represents the viscous damping (absent in our model). The first two terms are given by

$$I \simeq 1 - 3.5\ \frac{a}{h}, \quad Ka = \frac{2\pi a}{kh^2}. \tag{B2}$$

(Different forms of I have been proposed, and all converge to the same expression for subwavelength bubbles.)

Our model [Eqs. (48) and (49)] shows excellent agreement with Eqs. (B1) and (B2) for this specific case. Considering the expressions of $\Gamma_\circ$ for a sphere and Γ_{L} for a square lattice in Eq. (52), and the relation $d = V^{1/3}$ leading to Eq. (51), which, in particular, gives

$$\Gamma_\circ^{\mathrm{sph}} d = 4\pi a,$$

we obtain almost identical results. Specifically, for normal incidence, Eq. (48) involves

$$\left(1 - \Gamma_{\mathrm{L}}^{\mathrm{sq}} \Gamma_\circ^{\mathrm{sph}} \frac{d}{h}\right) = 1 - 3.9\frac{a}{h} \simeq I, \quad \kappa_x d = \frac{2\pi a}{kh^2} = Ka,$$

where there is only a minor shift in the resonance frequency. For completeness, we also refer to Lanoy *et al.* (2018), which uses the form of Eq. (50), where $\Omega = \omega/\omega_r$, $\omega_r = \omega_r^\infty/\sqrt{I}$, and

$$Q = \frac{2I}{Ka\Omega} = \frac{\sqrt{I}h^2\omega_r^\infty}{\pi c_\ell a}. \tag{B3}$$

Again, for normal incidence, our expression for Q in Eq. (14), using Eq. (2), leads to the same result as expected. In both references, viscous losses are introduced heuristically by considering $Ka \to Ka + \delta_{\mathrm{v}}$ or $1/Q \to 1/Q + 1/Q_{\mathrm{v}}$ in the denominator of R (with $T = 1 + R$), where

$$\delta_{\mathrm{v}} = \frac{4\eta}{\rho a^2 \omega}, \quad Q_{\mathrm{v}} = \frac{\rho_\ell a^2 \omega_r I}{2\eta}. \tag{B4}$$

This correction effectively accounts for the viscous losses associated with a single bubble (Devin, 1959; Prosperetti, 1977). Models that include viscous losses have been validated in numerous experimental studies but only for a rather limited range of bubble densities: $h/a = 5$ (Bretagne *et al.*, 2011) and $h/a = 4.5$ and 5.3 (Lanoy *et al.*, 2018). Only the study by Leroy *et al.* (2009) for $h = 3.5a$ and the more systematic investigation for decreasing values of h/a down to three (Leroy *et al.*, 2018), reveal the breakdown of the viscous model.

Following Leroy's model, the work of Skvortsov *et al.* (2019) is interesting as it raises the question of the role of lattice arrangement, which, as noted, has not been investigated in the literature. In this reference, $I = I^{\mathrm{sph}}$ (for spherical bubbles) is written in the form

$$I^{\mathrm{sph}} \simeq 1 - \gamma_{\mathrm{L}}^{\mathrm{sph}} \frac{a}{h}, \tag{B5}$$

which corresponds to Eq. (18) for small values of a/h, as reported in Table III of Skvortsov *et al.* (2019), where $\gamma_{\mathrm{L}}^{\mathrm{sph}}$ essentially corresponds to their parameter q_1. In our notation, $\gamma_{\mathrm{L}}^{\mathrm{sph}} a = \Gamma_\circ^{\mathrm{sph}} \Gamma_{\mathrm{L}} d$, hence, $\gamma_{\mathrm{L}}^{\mathrm{sph}} = 4\pi\Gamma_{\mathrm{L}}$. The parameter $\gamma_{\mathrm{L}}^{\mathrm{sph}}$ is evaluated through an interesting analogy between the notion of capacitance and the trapping rate of absorbing disks (Berezhkovskii *et al.*, 2006). However, the reported values of $\gamma_{\mathrm{L}}^{\mathrm{sph}}$ in Berezhkovskii *et al.* (2006) were obtained by fitting the numerical counterpart of I^{sph}, which makes it difficult to generalize them to other lattice arrangements beyond those considered (square, triangular, and hexagonal). Within this limitation, the results reported in Fig. 6 of Skvortsov *et al.* (2019) for square and triangular lattices show almost identical behaviors and are associated with significant errors, even for small values of a/h.

Alloul, M., Dollet, B., Stephan, O., Bossy, E., Quilliet, C., and Marmottant, P. (**2022**). "Acoustic resonance frequencies of underwater toroidal bubbles," Phys. Rev. Lett. **129**(13), 134501.
Ammari, H., Fitzpatrick, B., Gontier, D., Lee, H., and Zhang, H. (**2017a**). "A mathematical and numerical framework for bubble meta-screens," SIAM J. Appl. Math. **77**(5), 1827–1850.
Ammari, H., Fitzpatrick, B., Gontier, D., Lee, H., and Zhang, H. (**2017b**). "Sub-wavelength focusing of acoustic waves in bubbly media," Proc. R. Soc. A **473**(2208), 20170469.
Berezhkovskii, A. M., Monine, M. I., Muratov, C. B., and Shvartsman, S. Y. (**2006**). "Homogenization of boundary conditions for surfaces with regular arrays of traps," J. Chem. Phys. **124**(3), 036103.
Bouchet, D., Stephan, O., Dollet, B., Marmottant, P., and Bossy, E. (**2024**). "Near-field acoustic imaging with a caged bubble," Nat. Commun. **15**(1), 10275.
Boughzala, M., Stephan, O., Bossy, E., Dollet, B., and Marmottant, P. (**2021**). "Polyhedral bubble vibrations," Phys. Rev. Lett. **126**(5), 054502.
Bretagne, A., Tourin, A., and Leroy, V. (**2011**). "Enhanced and reduced transmission of acoustic waves with bubble meta-screens," Appl. Phys. Lett. **99**(22), 221906.

Caflisch, R. E., Miksis, M. J., Papanicolaou, G. C., and Ting, L. (**1985**). "Effective equations for wave propagation in bubbly liquids," J. Fluid Mech. **153**, 259–273.
Calvo, D. C., Thangawng, A. L., and Layman, C. N. (**2012**). "Low-frequency resonance of an oblate spheroidal cavity in a soft elastic medium," J. Acoust. Soc. Am. **132**(1), EL1–EL7.
Calvo, D. C., Thangawng, A. L., Layman, C. N., Casalini, R., and Othman, S. F. (**2015**). "Underwater sound transmission through arrays of disk cavities in a soft elastic medium," J. Acoust. Soc. Am. **138**(4), 2537–2547.
Delourme, B., Haddar, H., and Joly, P. (**2012**). "Approximate models for wave propagation across thin periodic interfaces," J. Math. Pures Appl. **98**(1), 28–71.
Devin, C., Jr. (**1959**). "Survey of thermal, radiation, and viscous damping of pulsating air bubbles in water," J. Acoust. Soc. Am. **31**(12), 1654–1667.
Euvé, L.-P., Pham, K., Petitjeans, P., Pagneux, V., and Maurel, A. (**2021**). "Time domain modelling of a Helmholtz resonator analogue for water waves," J. Fluid Mech. **920**, A22.
Feuillade, C. (**1995**). "Scattering from collective modes of air bubbles in water and the physical mechanism of superresonances," J. Acoust. Soc. Am. **98**(2), 1178–1190.
Hladky-Hennion, A.-C., and Decarpigny, J.-N. (**1991**). "Analysis of the scattering of a plane acoustic wave by a doubly periodic structure using the finite element method: Application to Alberich anechoic coatings," J. Acoust. Soc. Am. **90**(6), 3356–3367.
Lanoy, M., Guillermic, R.-M., Strybulevych, A., and Page, J. H. (**2018**). "Broadband coherent perfect absorption of acoustic waves with bubble metascreens," Appl. Phys. Lett. **113**(17), 171907.
Lanoy, M., Pierrat, R., Lemoult, F., Fink, M., Leroy, V., and Tourin, A. (**2015**). "Subwavelength focusing in bubbly media using broadband time reversal," Phys. Rev. B **91**(22), 224202.
Lebbe, N., Maurel, A., and Pham, K. (**2023**). "Homogenized transition conditions for plasmonic metasurfaces," Phys. Rev. B **107**(8), 085124.
Leroy, V., Chastrette, N., Thieury, M., Lombard, O., and Tourin, A. (**2018**). "Acoustics of bubble arrays: Role played by the dipole response of bubbles," Fluids **3**(4), 95.
Leroy, V., Strybulevych, A., Lanoy, M., Lemoult, F., Tourin, A., and Page, J. H. (**2015**). "Superabsorption of acoustic waves with bubble metascreens," Phys. Rev. B **91**(2), 020301.
Leroy, V., Strybulevych, A., Scanlon, M., and Page, J. H. (**2009**). "Transmission of ultrasound through a single layer of bubbles," Eur. Phys. J. E **29**(1), 123–130.
Marigo, J.-J., and Maurel, A. (**2016**). "Homogenization models for thin rigid structured surfaces and films," J. Acoust. Soc. Am. **140**(1), 260–273.
Marigo, J.-J., Pham, K., Maurel, A., and Guenneau, S. (**2021**). "Effective model for elastic waves in a substrate supporting an array of plates/beams with flexural and longitudinal resonances," J. Elast. **146**(1), 143–177.
Martin, P. (**2019**). "Acoustic scattering by one bubble before 1950: Spitzer, Willis, and Division 6," J. Acoust. Soc. Am. **146**(2), 920–926.
Martin, P., and Skvortsov, A. (**2020**). "Scattering by a sphere in a tube, and related problems," J. Acoust. Soc. Am. **148**(1), 191–200.
Maurel, A., Mercier, J.-F., Pham, K., Marigo, J.-J., and Ourir, A. (**2019**). "Enhanced resonance of sparse arrays of Helmholtz resonators—Application to perfect absorption," J. Acoust. Soc. Am. **145**(4), 2552–2560.
Miksis, M. J., and Ting, L. (**1989**). "Effects of bubbly layers on wave propagation," J. Acoust. Soc. Am. **86**(6), 2349–2358.
Minnaert, M. (**1933**). "On musical air-bubbles and the sounds of running water," London, Edinburgh, Dublin Philos. Mag. J. Sci. **16**(104), 235–248.
Pham, K., Maurel, A., and Marigo, J.-J. (**2021a**). "Revisiting imperfect interface laws for two-dimensional elastodynamics," Proc. Math. Phys. Eng. Sci. **477**(2245), 20200519.
Pham, K., Mercier, J.-F., Fuster, D., Marigo, J.-J., and Maurel, A. (**2021b**). "Scattering of acoustic waves by a nonlinear resonant bubbly screen," J. Fluid Mech. **906**, A19.
Prosperetti, A. (**1977**). "Thermal effects and damping mechanisms in the forced radial oscillations of gas bubbles in liquids," J. Acoust. Soc. Am. **61**(1), 17–27.
Schnitzer, O., and Brandão, R. (**2022**). "Absorption characteristics of large acoustic metasurfaces," Philos. Trans. R. Soc. A **380**(2231), 20210399.
Skvortsov, A., MacGillivray, I., Sharma, G. S., and Kessissoglou, N. (**2019**). "Sound scattering by a lattice of resonant inclusions in a soft medium," Phys. Rev. E **99**(6), 063006.
Smythe, W. R. (**1950**). *Static and Dynamic Electricity*, 3rd ed. (McGraw-Hill, New York).
Spratt, K. S., Hamilton, M. F., Lee, K. M., and Wilson, P. S. (**2017**). "Radiation damping of, and scattering from, an arbitrarily shaped bubble," J. Acoust. Soc. Am. **142**(1), 160–166.
Strasberg, M. (**1953**). "The pulsation frequency of nonspherical gas bubbles in liquids," J. Acoust. Soc. Am. **25**(3), 536–537.
Tachet, S., Pham, K., and Maurel, A. (**2025**). "Homogenized models of acoustic metainterfaces made of three-dimensional Helmholtz resonators," Proc. R. Soc. A **481**(2316), 20241000.
Thieury, M., Leroy, V., Dassé, J., and Tourin, A. (**2020**). "Phenomenological law for the acoustic reflection by an array of cylindrical cavities in a soft elastic medium," J. Appl. Phys. **128**(13), 135106.
Ye, Z. (**1997**). "Resonant scattering of acoustic waves by ellipsoid air bubbles in liquids," J. Acoust. Soc. Am. **101**(2), 681–685.